



Investigation on the pyrolysis and oxidation of toluene over a wide range conditions. I. Flow reactor pyrolysis and jet stirred reactor oxidation

Wenhai Yuan ^{a,b}, Yuyang Li ^{a,*}, Philippe Dagaut ^{b,*}, Jiuzhong Yang ^c, Fei Qi ^{a,c}

^a State Key Laboratory of Fire Science, University of Science and Technology of China, Hefei, Anhui 230026, PR China

^b CNRS-I.N.S.I.S., Institut de Combustion, Aérothermique, Réactivité et Environnement, 1C, Avenue de la Recherche Scientifique, 45071 Orléans Cedex 2, France

^c National Synchrotron Radiation Laboratory, University of Science and Technology of China, Hefei, Anhui 230029, PR China



ARTICLE INFO

Article history:

Received 7 April 2014

Received in revised form 5 July 2014

Accepted 12 July 2014

Available online 14 August 2014

Keywords:

Toluene

Pyrolysis

Oxidation

Kinetic model

PAH formation

ABSTRACT

The pyrolysis of toluene was studied in a flow reactor at pressures from 5 to 760 Torr and temperatures from 1100 to 1730 K using synchrotron vacuum ultraviolet photoionization mass spectrometry. The pyrolysis species and intermediates, including some radicals, isomers and large PAHs, were identified and their mole fraction profiles were evaluated as the function of heating temperature. The oxidation of toluene was investigated in a jet stirred reactor (JSR) at the pressure of 10 atm, residence time of 0.6 s, equivalence ratios of 0.5, 1.0 and 1.5, and temperatures from 950 to 1200 K using gas chromatography combined with flame ionization detector, thermal conductivity detector and mass spectrometry. The concentration profiles of oxidation products as the function of heating temperature were measured. Based on recent theoretical progresses, a detailed kinetic model of toluene combustion with 272 species and 1698 reactions was developed to reproduce the decomposition of toluene and growth of aromatics in both the flow reactor pyrolysis and JSR oxidation. The rate of production analysis and the sensitivity analysis reveal that benzyl and fulvenallenyl radicals play crucial roles in the decomposition of toluene and formation of polycyclic aromatic hydrocarbons (PAHs).

© 2014 The Combustion Institute. Published by Elsevier Inc. All rights reserved.

1. Introduction

Aromatic hydrocarbons are major components of petroleum-based transportation fuels and are widely used as major components of surrogate fuels for gasoline, diesel oil and kerosene. They are also key precursors of soot which is an important combustion-derived air pollutant known to be harmful to both the environment and human health [1]. Consequently, understanding the combustion chemistry of aromatic hydrocarbons is crucial for the development of kinetic models of surrogate fuels, and increases our knowledge on the gas phase molecular growth process in soot formation mechanism. As the simplest alkylated aromatic hydrocarbon, toluene is one of the most abundant aromatic components in gasoline [2] and a typical component in gasoline surrogate fuels [3,4]; it also serves to improve the anti-knock properties of gasoline. The kinetic model of toluene combustion is also widely used to develop kinetic models of large aromatic components in diesel and kerosene surrogate fuels. Furthermore, its major initial decomposition product, benzyl radical, is recognized as a key intermediate

involved in the formation of polycyclic aromatic hydrocarbons (PAHs) and soot [5–8]. Thus, experimental and kinetic modeling research on the pyrolysis and oxidation of toluene is of great importance among the combustion studies of aromatic hydrocarbons.

Many experimental studies on the pyrolysis and oxidation of toluene have been performed, providing a large body of experimental data for the validation of toluene models. Concentration profiles of species in pyrolysis [8–19], oxidation [20–29] and flames [6,30–33] of toluene have been measured. The pioneering work of toluene pyrolysis was performed by Smith [9] in a Knudsen cell at a very low pressure using electron-impact ionization (EI) mass spectrometry (MS). Subsequently, Pamidimukkala et al. [10], Colket and Seery [11] and Sivaramakrishnan et al. [13,14] performed shock tube pyrolysis studies of toluene. Pamidimukkala et al. [10] investigated the pyrolysis of toluene at temperatures of 1550–2200 K and pressures from 0.2 to 0.5 atm, and the mole fractions of some products were measured as the function of reaction time using time-of-flight (TOF) MS and laser-schlieren densitometry. Colket and Seery [11] studied the pyrolysis of toluene at 10 atm, and observed many stable products using gas chromatography (GC), including some PAHs. The work of Sivaramakrishnan et al. [13,14] was performed at 27 and 45 bar over a wide temperature range (1200–1900 K). Some stable species were detected

* Corresponding author.

E-mail addresses: yugli@ustc.edu.cn (Y. Li), dagaut@cnrs-orleans.fr (P. Dagaut).

using GC combined with MS (GC-MS). A more recent work on the pyrolysis of toluene was performed by Zhang et al. [16] in a flow reactor at 10 Torr using synchrotron vacuum ultraviolet photoionization mass spectrometry (SVUV-PIMS).

A detailed description of the previous studies on the oxidation of toluene has been reviewed by Metcalfe et al. [29], thus not repeated herein. Generally, most of previous oxidation studies of toluene were performed in flow reactors [20–23,29], jet stirred reactors (JSR) [24,27] and shock tubes [26,28]. Brezinsky et al. [20,21], Emdee et al. [22] and Klotz et al. [23] performed the oxidation of toluene in a turbulent flow reactor at 1 atm, ~1200 K and equivalence ratios (ϕ) from 0.69 to 1.33 using GC-MS. Metcalfe et al. [29] studied the oxidation of toluene in a turbulent flow reactor at 12.5 atm and 420–950 K using Fourier transform infrared (FTIR) spectroscopy and GC. Dagaut et al. [24] investigated the JSR oxidation of toluene at 1 atm, 1000–1375 K and various equivalence ratios (0.5–1.5) using on-line and off-line GC methods. Bounaceur et al. [27] studied the JSR oxidation of toluene at 1 atm, 873–923 K and equivalence ratios from 0.45 to 0.91 using GC-MS. Hamins and Seshadri [30] investigated the counterflow diffusion toluene flames. Some major flame species were detected using GC, and their mole fraction profiles were evaluated. Detilleux and Vandooren [31,33] studied laminar premixed flames of toluene at 36 Torr and equivalence ratios from 0.7 to 2.0 using GC combined with molecular beam mass spectrometry (MBMS). Li et al. [6,32] studied the laminar premixed toluene flames at 30 Torr and a variety of equivalence ratios (0.75–1.90) using SVUV-PIMS.

Global combustion parameters of toluene such as ignition delay times [27,34–40] and laminar flame speeds [41–47] have also been measured. Metcalfe et al. [29] have reviewed the previous measurements of ignition delay times of toluene. The recent review of Ranzi et al. [48] summarizes the experimental work on laminar flame speeds of toluene before 2012. Thus descriptions of these previous studies are not repeated herein. Recently, Hui et al. [44], Ji et al. [45] and Sileghem et al. [46] performed new experimental studies on the laminar flame speeds of toluene. Hui et al. determined the laminar flame speeds of toluene at 1 atm and the initial temperatures of 400 and 470 K. Ji et al. determined the laminar flame speeds of toluene at 1 atm and the initial temperature of 353 K. Sileghem et al. determined the laminar flame speeds of toluene at 1 atm and the initial temperatures from 298 to 358 K.

There are also numerous theoretical studies [49–61] on the reactions involving toluene and its decomposition products, such as benzyl radical, fulvenallene and fulvenallenyl radical, which will be introduced in detail in the Kinetic Model Development section. Based on the experimental and theoretical studies, several kinetic models of toluene have also been developed. Detailed introduction of these models can be found in the work of Metcalfe et al. [29]. Emdee et al. [22] developed a kinetic model of toluene oxidation and validated the model against their flow reactor oxidation data. Dagaut et al. [24] proposed a kinetic model of toluene oxidation based on their JSR oxidation data and also validated against ignition delay times and laminar flame speeds. Narayanaswamy et al. [7] proposed a high temperature oxidation model of substituted aromatics, which was validated against the oxidation data in flow reactor, ignition delay times and laminar flame speeds of toluene. Recently, Metcalfe et al. [29] proposed a toluene oxidation model and validated it against a variety of oxidation data and global combustion parameters. It should be noted that all these models concern toluene oxidation and most of them were not validated over a wide range of conditions. Furthermore, very few of them include the chemistry of aromatic growth which includes the growth of monocyclic aromatic hydrocarbons (MAHs) and the formation and growth of PAHs.

It is recognized that systematic investigations on toluene pyrolysis at various pressures and toluene oxidation at high pressures are

still insufficient, and a kinetic model widely validated against both pyrolysis and oxidation data of toluene is lacking. Further experimental and modeling efforts are needed in order to achieve a comprehensive exploration on the pyrolysis and oxidation of toluene. Consequently, this work investigates the flow reactor pyrolysis of toluene at pressures from 5 to 760 Torr using SVUV-PIMS and the JSR oxidation of toluene at 10 atm and three equivalence ratios (0.5, 1.0 and 1.5) using GC combined with flame ionization detector (FID), thermal conductivity detector (TCD) and MS. Based on recent theoretical progresses, a toluene model consisting of 272 species and 1698 reactions was developed and validated against the present pyrolysis and oxidation data. Modeling analyses were performed to provide insight into the chemistry of fuel decomposition and aromatic growth.

2. Experimental methods

2.1. Flow reactor pyrolysis

The flow reactor pyrolysis experiments were performed at National Synchrotron Radiation Laboratory in Hefei, China. The beamlines used in this work have been introduced in detail elsewhere [32,62]. The detailed description of the pyrolysis apparatus can be found in our recent work [63–65]. In brief, the experimental apparatus consists of a pyrolysis chamber with an electrically heated flow reactor, a differentially pumped chamber with a molecular beam sampling system, and a photoionization chamber with a home-made reflectron TOF mass spectrometer (RTOF-MS). The pressures in the pyrolysis chamber were maintained at 5, 30, 80, 200 and 760 Torr, respectively. Toluene was purchased from Sinopharm Chemical Reagent Limited Co., Shanghai, China, with a purity of 99.5%. During the experiment, the gas mixture of toluene (50 standard cubic centimeters per minute, sccm) and Ar (950 sccm) was fed into the flow tube in the reactor with a heated length of 150 mm. The flow tube was made of α -alumina to reduce wall catalytic effects [66,67]. For the modeling purpose, a small inner diameter (6.8 mm) was used to ensure strong radial diffusion effects, reduce radial concentration gradients and achieve adequately homogeneous reaction circumstances according to the experiences in previous laminar flow reactor experiments [68–70]. The pyrolysis products were then sampled at 10 mm downstream from the outlet by a quartz nozzle. The formed molecular beam passed through a nickel skimmer, and then was ionized by the synchrotron light at the ionization region. The ion signals were recorded by the RTOF-MS.

The methods of centerline temperature measurement and pressure distribution calculation were also described in detail elsewhere [63,65], and are briefly introduced in the **Supplementary Materials**. The centerline temperature profiles are provided in the **Supplementary Materials**. Each temperature profile was named by its maximum value (T_{max}) which will be used in the experimental and simulated results. The uncertainty of T_{max} is estimated to be within ± 30 K. For a pressure above 30 Torr, the pressure decrease from the inlet of the reactor to the outlet is less than 10%, so the centerline pressure distribution can be treated as a constant value. The pressure profiles at 5 Torr and different T_{max} s are also provided in the **Supplementary Materials**.

Two experimental modes were used in this work. At each pressure, photoionization efficiency (PIE) spectra were measured to provide information on ionization energies for the identification of pyrolysis products; mass spectra at some selected photon energies were recorded at a variety of T_{max} s to deduce mole fraction profiles of pyrolysis species. The data evaluation method has been reported previously [65] and will not be repeated here. The uncertainties of evaluated mole fractions are estimated to be within

±25% for pyrolysis products with known photoionization cross sections (PICSS), and a factor of 2 for those with estimated PICSS. The PICSS of pyrolysis products are available in the online database [71].

2.2. Jet stirred reactor oxidation experiment

The JSR oxidation experiments were performed at C.N.R.S.-I.N.S.I.S. in Orléans, France. The experiment was performed at 10 atm, 950–1200 K and three equivalence ratios (0.5, 1.0 and 1.5). A high-pressure liquid chromatography pump (Hewlett Packard 1100) was used to deliver sonically degassed toluene (99.8% purity, Sigma Aldrich) to an atomizer-vaporizer assembly maintained at 150 °C. A high degree of dilution (0.1% volume of fuel) was used in order to reduce the temperature gradients in the reactor caused by the oxidation heat release. High-purity oxygen (99.995% pure) was used in these experiments. The reactants were diluted by high-purity nitrogen (<50 ppm O₂, <1000 ppm Ar, <5 ppm H₂) and mixed at the entrance of the injectors. All the gases were preheated before injection to minimize temperature gradients inside the reactor.

The jet stirred reactor and the experimental procedure used in this work are similar to what were used earlier [72]. The reactor consists of a small fused silica sphere of 40 mm inner diameter (30.5 cm³). Four nozzles of 1 mm inner diameter were mounted in the sphere to feed the gases and achieve stirring. A regulated heating wire of ca. 1.5 kW maintained the temperature of the reactor at the desired working temperature. Good thermal homogeneity along the whole vertical axis of the reactor (gradients of ca. 1 K/cm) was observed for each experiment by thermocouple (0.16 mm chromel-alumel) measurements (typical change ≤5 K). The reacting mixtures were sampled by means of a fused silica low-pressure sonic probe. The samples were analyzed on-line by GC-MS-FID and off-line after collection and storage in 1 L Pyrex bulbs. Off-line analysis was done using GC equipped with capillary columns (DB-5 ms, Al₂O₃-KCl, Poraplot U and Carboplot-P7), a TCD and an FID.

3. Kinetic model development

The present kinetic model for the pyrolysis and oxidation of toluene (A1CH₃, the nomenclature in this model) at various pressures consists of 272 species and 1698 reactions. Table S1 in the Supplementary Materials lists the rate constants of some key reactions in this model and their sources. Table S2 in the Supplementary Materials lists the molecular weights, formulas, names, nomenclatures in this model and molecular structures for the C₅ and larger species mentioned below. Our previously reported low-pressure toluene combustion model [6,18] was used as a start point to develop this model. The reaction mechanism mainly consists of the sub-mechanisms of toluene, benzene (A1), 1,3-cyclopentadiene (C₅H₆), C₆–C₈ species and C₈ and larger aromatic species. A number of key reactions were updated from recent theoretical studies, especially for some important pressure-dependent unimolecular decomposition reactions and chemically activated reactions. The construction of the toluene sub-mechanism and the large aromatics sub-mechanism will be described in detail below.

3.1. Toluene sub-mechanism

3.1.1. Unimolecular decomposition of toluene

The unimolecular decomposition of A1CH₃ can produce benzyl (A1CH₂), phenyl (A1–) and methylphenyl (C₆H₄CH₃) radicals through (R1–R3), respectively. The pressure-dependent rate constants of R1 and R2 were theoretically investigated by Klippenstein

et al. [50]. Their calculated rate constants and branching ratios were experimentally validated by Sivararamakrishnan et al. [73] in the shock tube pyrolysis of C₆D₅CH₃. A more recent theoretical study of these reactions by Lefort and Tsang [58] only shows slight discrepancies with the results of Klippenstein et al. Therefore, the results of Klippenstein et al. were adopted in this model. Due to the lack of theoretical and experimental investigations, the rate constant of R3 was assumed by analogy with the reaction of A1 [74].



3.1.2. Bimolecular decomposition and oxidation of toluene

The H-atom abstraction reactions of A1CH₃ by H can produce A1CH₂ (R4) and C₆H₄CH₃ (R5). In this model, the rate constant measured by Oehlschlaeger et al. [75] was used for R4, while the estimated rate constant by Bounaceur et al. [27] was used for R5. The ipso-substitution reaction of A1CH₃ (R6) by H can form A1 and methyl radical (CH₃). The rate constant recommended by Vasu et al. [40] was used in this model. The H-atom abstraction reactions of A1CH₃ by CH₃ to produce A1CH₂ and C₆H₄CH₃ were taken from the model of Blanquart et al. [76].



Similar to the reactions between A1CH₃ and H, the reactions between A1CH₃ and OH also include the H-atom abstraction reactions to produce A1CH₂ (R7) and C₆H₄CH₃ (R8) and the ipso-substitution reaction to produce phenol (A1OH, R9). Cresol (HOCH₂CH₃) can also be produced by replacing an H atom on the benzene ring of A1CH₃ (R10). Seta et al. [49] measured the rate constants of these reactions, which were adopted in this model.



The reactions of A1CH₃ with O are more complicated than those with OH, and are lack of theoretical and experimental investigations. Besides the formation of A1CH₂ (R11) and C₆H₄CH₃ (R12), the reaction between A1CH₃ and O can also produce methylphenoxyl radical (OC₆H₄CH₃, R13), cresol (R14) and methylcyclopentadiene (C₅H₅CH₃, R15). In this model, R11 and R12 were taken from the models of Blanquart et al. [76] and Bounaceur et al. [27], respectively. For the other three reactions (R13)–(R15), their rate constants were estimated by analogy with the similar reactions between A1 and O investigated by Taatjes et al. [77].



Furthermore, the H-atom abstraction of A1CH₃ by O₂ mainly takes place at the CH₃ group and produces A1CH₂ and HO₂ (R16). Oehlschlaeger et al. [78] investigated R16 in shock tube, and their measured rate constant was used in this model. The H-atom abstraction reactions of A1CH₃ by HO₂ can also produce A1CH₂ and C₆H₄CH₃. For the former reaction, we adopted the rate

constant recommended by Baulch et al. [79], while the later reaction was referred to the analogous reaction of A1 calculated by Altarawneh et al. [80].



3.1.3. Decomposition and oxidation of benzyl radical

Numerous studies have been performed on the decomposition of A1CH₂ in the last decades. Smith [9] and Colket and Seery [11] proposed that A1CH₂ mainly decomposes via two non-atom producing pathways to form cyclopentadienyl radical (C₅H₅) + acetylene (C₂H₂) (R17) and propargyl radical (C₃H₃) + vinylacetylene (C₄H₄), which was widely adopted in many previous toluene models. However, recent experimental [12,15,16,31,32,75] and theoretical [18,51,53–57,59,60,81–83] studies have revealed that fulvenallene (C₇H₆) is an abundant and important intermediate in the decomposition of A1CH₃ and A1CH₂, and the H-atom removal from the benzene ring (R18) to produce C₇H₆ shows great significance compared with the most favored non-atom producing pathway (R17). For example, da Silva et al. [53] found that R17 has a 6.8 kcal/mol higher energy barrier than R18. Recently, Derudi et al. [57] theoretically investigated another non-atom producing pathway yielding benzyne (o-C₆H₄) + CH₃ (R19). In the present model, these recent findings were considered for describing the chemistry of A1CH₂ decomposition. The pressure-dependent rate constants of R18 and R19 calculated by Derudi et al. [57] were adopted. Furthermore, A1CH₂ can also react with H to produce A1– and CH₃ (R20). The pressure-dependent rate constant of R20 calculated by Klippenstein et al. [50] was used in this model.



The oxidation of A1CH₂ proceeds mainly via the reactions with OH, O, HO₂ and O₂. The reaction between A1CH₂ and OH can produce benzyl alcohol (A1CH₂OH). In this model, the rate constant was estimated by analogy with the reaction between CH₃ and OH to form methanol (CH₃OH). The subsequent reactions of A1CH₂OH leading to benzoyl radical (A1CH₂O) were adopted from the model of Narayanaswamy et al. [7]. The reaction between A1CH₂ and O to form A1CH₂O was also taken from the model of Narayanaswamy et al. [7]. As proposed by da Silva et al. [52], the reactions between A1CH₂ and HO₂ radicals produce A1CH₂O (R21) and benzyl hydroperoxide (A1CH₂OOH), and their calculated rate constants were used in this model. The reactions between A1CH₂ radical and O₂ to produce benzylperoxy radical (A1CH₂OO), benzaldehyde (A1CHO, R22) and phenoxy radical (A1O) were investigated by Murakami et al. [84], and their calculated rate constants were used in this model. Furthermore, the rate constants for the unimolecular decomposition reactions of A1CH₂O to produce A1CHO + H, A1 + HCO and A1– + CH₂O were taken from the theoretical work of da Silva et al. [85]. The rate constant for the H-atom abstraction of A1CH₂O by O₂ was taken from the model of Bounaceur et al. [27], and the rate constants of the other H-atom abstraction reactions of A1CH₂O were adopted from the model of Narayanaswamy et al. [7].



3.1.4. Decomposition and oxidation of methylphenyl radical

As demonstrated by Derudi et al. [57], the unimolecular decomposition of C₆H₄CH₃ can produce o-C₆H₄. In this model, its rate constant was estimated from the analogous reaction A1– = o-C₆H₄ + H

calculated by Madden et al. [86]. C₆H₄CH₃ can also convert to A1CH₂ via unimolecular isomerization and bimolecular H-assisted isomerization. The corresponding rate constants were taken from the theoretical work of Dames and Wang [87] and the model of Bounaceur et al. [27], respectively.

For the oxidation reactions of C₆H₄CH₃, the reactions between C₆H₄CH₃ and O₂ (e.g. R23) were adopted from the theoretical work of da Silva et al. [88], and those of C₆H₄CH₃ with OH, O and HO₂ were taken from the model of Bounaceur et al. [27]. The oxidation reactions of C₆H₄CH₃ mainly produce methylphenoxy radical (OC₆H₄CH₃) which can lead to methylcyclopentadienyl radical (C₅H₄CH₃) + CO by unimolecular decomposition (R24) or cresol by adding an H atom. The rate constant of R24 was estimated from the analogous reaction of A1O calculated by You et al. [89], and that of the H addition was estimated from the analogous reaction A1O + H = A1OH [90].



3.1.5. Decomposition and oxidation of C₇H₆ and C₇H₅

Fulvenallene is calculated to be the more stable C₇H₆ species [54] and has been unambiguously distinguished in toluene pyrolysis and flames [6,16,32]. Its two main unimolecular decomposition pathways produce C₇H₅ + H (R25) and cyclopentadienylidene (cC₅H₄) + C₂H₂ (R26). Their rate constants calculated by Polino et al. [59] were adopted in this model. The rate constants of H-atom abstraction reactions of C₇H₆ to form C₇H₅ were taken from the theoretical work of da Silva et al. [51], and that of the reaction between C₇H₆ and H yielding C₅H₅ + C₂H₂ (R27) was taken from another theoretical study of da Silva et al. [54]. The rate constants of the two main unimolecular decomposition reactions of C₇H₅ to produce diacetylene (C₄H₂) + C₃H₃ (R28) and C₅H₃ radical (H₂CCCC*H) + C₂H₂ (R29) were taken from the theoretical work of Derudi et al. [57].



3.2. Large aromatics sub-mechanism

3.2.1. Formation and consumption of MAHs

The important MAHs with molecular weights larger than fuel in toluene combustion include phenylacetylene (A1C₂H), styrene (A1C₂H₃) and ethylbenzene (A1C₂H₅). A1C₂H can be produced either from the C₂H₂ addition reaction on A1– [74] or from the stepwise H-atom elimination reactions of A1C₂H₃ [74]. A1C₂H₃ can be generated from the stepwise H-atom elimination of A1C₂H₅ [74]. In addition, the decomposition of stilbene (C₁₄H₁₂) [8] and the reaction between C₅H₅ and C₃H₃ (R30) [6,91] can also produce A1C₂H₃. A1C₂H₅ can be produced from the combination of A1CH₂ and CH₃. In the present model, the rate constants of the formation and consumption reactions of these MAHs were mainly taken from previous models [6,8,74,76,91] or estimated by analogy with the similar reactions.



3.2.2. Formation and consumption of bicyclic PAHs

Indene (C₉H₈) is the simplest bicyclic PAH and is abundantly produced in the combustion of aromatic fuels. It can be formed

from the reaction between A1CH₂ and C₂H₂ (R31). The rate constant of this reaction was taken from the theoretical work of Vereecken et al. [92]. The reactions of o-C₆H₄, A1⁻ and A1 with C₃ species [6,92,93] can also produce C₉H₈. Besides these pathways, C₉H₈ was also proposed to be produced from the reaction between C₅H₅ and C₃H₆ (R32) by Kislov and Mebel [94] and Cavalotti et al. [61] and the reaction between C₇H₆ and C₂H₂ by da Silva and Bozzelli [51]. The rate constants of H-atom abstraction reactions of C₉H₈ to produce indenyl radical (C₉H₇) were mainly taken from the model of Blanquart et al. [76], while that of its unimolecular decomposition reaction to produce C₉H₇ was estimated from the similar reaction of C₅H₆. The reactions of A1⁻, o-C₆H₄ and A1 with C₃ species [6,8] and the reactions of C₇H₅ and C₇H₆ with C₂ species [51] can also produce C₉H₇, which were considered in the present model.



In most of previous studies, naphthalene is considered to be mainly produced from the reaction between A1CH₂ and C₃H₃. Recently, Matsugi and Miyoshi [8,95] proposed a multistep mechanism for this global reaction: A1CH₂ + C₃H₃ → C₉H₇CH₂ (→C₉H₆CH₂) → A2. In this multistep mechanism, 1-methyleneindan-2-yl radical (C₉H₇CH₂) and methyleneindene (C₉H₆CH₂) are formed and then convert to A2 by unimolecular decomposition (R33) and isomerization (R34), respectively. In the present model, these pathways were considered with rate constants taken from the work of Matsugi and Miyoshi [8,95].



C₅ + C₅ reactions, i.e. C₅H₅ + C₅H₅ and C₅H₅ + C₅H₆, are other important pathways to the formation of naphthalene. In many previous studies [7,76,96,97], A2 is the main product of the self-combination reaction of C₅H₅. The recent study by Cavalotti and Polino [8] revealed that the self-combination of C₅H₅ mainly leads to two C₁₀H₉ radicals, i.e. azulyl and fulvalenyl (C₅H₅–C₅H₄) radicals. At temperatures below 1450 K, the formation of azulyl radical is dominant, while above 1450 K, the dominant product is fulvalenyl radical. The two C₁₀H₉ radicals were lumped as C₅H₅–C₅H₄ in this model. The rate constants of the formation and decomposition reactions of C₅H₅–C₅H₄ (R35), (R36) were taken from the theoretical work of Cavalotti and Polino [8] and Mebel and Kislov [98], respectively. For the reaction C₅H₅ + C₅H₆ to form A2, the rate constant was taken from the theoretical study of Cavalotti et al. [61]. Furthermore, da Silva and Bozzelli [51] proposed that C₇H₅ can react with C₃H₃ to produce A2 (R37) which was also considered in the present model. Other formation pathways of A2 include the reaction between o-C₆H₄ and A1 [99] and the C₆ + C₄ reactions [76].



The consumption of A2 occurs mainly via the H-atom abstraction reactions to form 1-naphthyl (A2-1) and 2-naphthyl (A2-2) radicals. In addition, the oxidation of A2 can produce naphthalenols (A2OH-1, A2OH-2), naphthalenoxyl radicals (A2O-1, A2O-2) and indene. The decomposition of naphthalenoxyl radicals will ultimately lead to C₉H₇ + CO (R38). Since rate constants are not available for most of these reactions, they were estimated from the similar reactions of A1.



Biphenyl (P2), diphenylmethane (C₁₃H₁₂) and bibenzyl (C₁₄H₁₄) are three important bicyclic PAHs without fused aromatic rings. The formation reactions of P2 include the self-combination reaction of A1⁻ and the reaction between A1 and A1⁻. The reaction between C₇H₅ + C₅H₅ may also contribute to the formation of P2, as proposed by da Silva and Bozzelli [51]. The formation reactions of C₁₃H₁₂ and C₁₄H₁₄ include the combination reaction of A1⁻ + A1CH₂ and the self-combination reaction of A1CH₂. These reactions were considered in the present model with rate constants taken from Refs. [6,74,91,100] or estimated from the similar reactions.

3.2.3. Formation and consumption of tricyclic and tetracyclic PAHs

Acenaphthylene (A2R5) has two fused benzene rings and one fused five-number ring. It can be formed from the reaction between C₉H₇ and C₃H₃ (R39) [76,96], the C₂H₂ addition to A2-1 [74] and the reaction sequence originated from P2 [101]. These reactions were considered with rate constants taken from the previous models [74,76,101].



The decomposition of C₁₃H₁₂ can produce diphenylmethyl radical (C₁₃H₁₁). The subsequent decomposition of C₁₃H₁₁ forms fluorene (C₁₃H₁₀). Matsugi and Miyoshi [102] studied these reactions theoretically and their calculated rate constants were used here. C₁₃H₁₀ can loss an H atom to produce fluorenyl radical (C₁₃H₉).

Phenanthrene (A3) can be produced via a variety of pathways in the pyrolysis and oxidation of toluene. As investigated earlier [6,8,18,19], A3 can be produced from the reaction sequence: C₁₄H₁₄ → C₁₄H₁₃ → C₁₄H₁₂ → C₁₄H₁₁ → A3. In this model, the rate constants of these reactions were taken from the theoretical investigation of Matsugi and Miyoshi [8]. Another important pathway suggested by da Silva and Bozzelli [51] for the formation of A3 is the self-combination reaction of C₇H₅ (R40), which is also considered in the present model with the rate constant estimated from the similar reaction of C₃H₃. The decomposition of hydro-methylenefluorene radical (C₁₃H₉CH₂) can also contribute to the formation of A3 (R41) [8]. C₁₃H₉CH₂ can be produced either from fluorene in the sequence C₁₃H₁₀ → C₁₃H₉ → C₁₃H₉CH₂ or from the reaction of A1CH₂ and C₇H₅, and both pathways were considered in this model. The main consumption pathways of A3 are similar to those of A2. Moreover, A3 can isomerize to anthracene (A3L) in combustion [11].



There are only few studies on the formation of pyrene (A4) and chrysene (CHRYSEN) in the combustion of toluene and other aromatic fuels [74,96]. The formation of A4 can occur via reactions of 4-phenanthrenyl radical (A3-4) + C₂H₂, C₁₃H₉ + C₃ species and A1⁻ + A2. The formation of chrysene can occur via the self-combination reaction of C₉H₇ and the reaction between A2-2 and A1C₂H. These pathways were considered in the present model with rate constants taken from the previous models [74,96] or estimated from the similar reactions.

3.3. Thermodynamic data and transport data

Most of the thermodynamic and transport data of C₀–C₆ species used in this work were taken from the USC Mech II model [103] and our previous work [104]. Most of the thermodynamic data of aromatic species were taken from Refs. [8,74,76,96,105]. The reaction mechanism, thermodynamic data and transport data are provided in the *Supplementary Materials*.

4. Results and discussion

4.1. Flow reactor pyrolysis

Dozens of pyrolysis products were detected in the flow reactor pyrolysis experiments, and their mole fraction profiles as the function of heating temperature were also measured. The simulation was performed with the Plug Flow Reactor module in the Chemkin-Pro software [106]. A detailed description of the simulation method has been introduced in our recent work [104]. The measured temperature profiles were used to simulate the flow reactor pyrolysis at all five pressures, while the calculated pressure profiles were used in the simulation of the 5 Torr experiment, as introduced in Section 2.1. The experimental and simulated mole fraction profiles of pyrolysis species are shown in Figs. 1–5. In general, this model can capture the decomposition or formation temperatures of observed pyrolysis species and reproduce their mole fraction profiles within the experimental uncertainties. Some modeling analysis tools including the rate of production (ROP) analysis and the sensitivity analysis were used to provide insight into the chemistry of toluene decomposition and aromatics growth.

4.1.1. Toluene decomposition

4.1.1.1. Primary decomposition of toluene. Figure 1 presents the experimental and simulated mole fraction profiles of A1CH_3 , A1CH_2 , C_7H_6 , C_7H_5 , A1 and $\text{o-C}_6\text{H}_4$ at five pressures. Based on the ROP analysis, the reaction networks in the decomposition of

A1CH_3 at pressures of 5 and 760 Torr were drawn in Fig. 6. The primary decomposition of A1CH_3 at pyrolysis conditions is dominated by three types of reactions, that is, the unimolecular decomposition (R1)–(R3), the H-atom abstraction (e.g. R4, R5) and the ipso-substitution by H (R6). Based on the ROP analysis, their contributions to the decomposition of A1CH_3 vary with temperature and pressure, as illustrated in Fig. 7. Figure 7(a) compares their contributions at 5 Torr and different temperatures. At the low temperatures when A1CH_3 just starts to decompose, the unimolecular decomposition consumes most of A1CH_3 , while as the temperature increases, the contribution of unimolecular decomposition decreases and that of H-atom abstraction increases. This can be explained by the fact that chain propagation reactions rely on the radicals provided by chain initiation reactions. It is also observed that the contribution of ipso-substitution is not very sensitive to the variation of temperature, and locates around 15% at all temperatures. To reveal the effect of pressure on the contributions of different types of reactions, the ROP analysis was performed at the temperatures of ~50% predicted conversion of A1CH_3 , that is, 1600 K for 5 Torr, 1500 K for 30 Torr, 1450 K for 80 Torr, 1400 K for 200 Torr and 1350 K for 760 Torr. It is noted that the ROP analysis and sensitivity analysis in the following discussion of Section 4.1 are also performed at these temperatures. The results are presented in Fig. 7(b). As the pressure increases, the contributions of H-atom abstraction and ipso-substitution increase, while that of unimolecular decomposition decreases.

The unimolecular decomposition of A1CH_3 produces A1CH_2 (R1), A1 –(R2) and $\text{C}_6\text{H}_4\text{CH}_3$ (R3). Due to the at least 10 kcal/mol lower bond dissociation energy (BDE) of methyl C–H bonds than

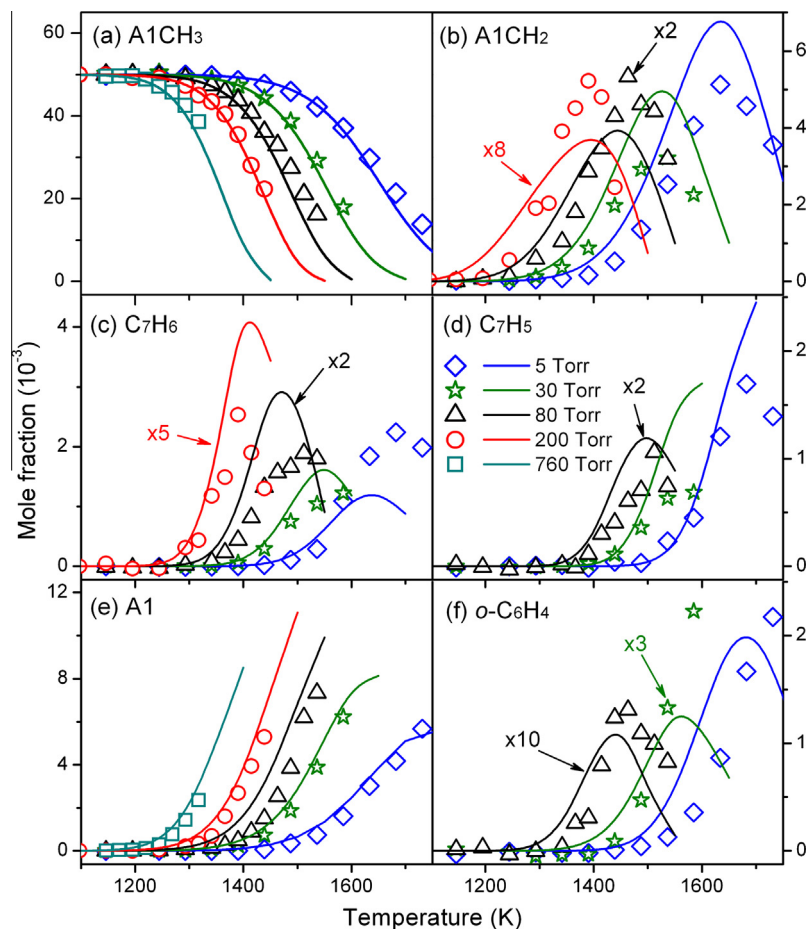


Fig. 1. Experimental (symbols) and simulated (lines) mole fraction profiles of toluene (A1CH_3), benzyl radical (A1CH_2), fulvenallene (C_7H_6), fulvenallenyl radical (C_7H_5), benzene (A1) and benzene ($\text{o-C}_6\text{H}_4$) in the flow reactor pyrolysis of toluene at different pressures.

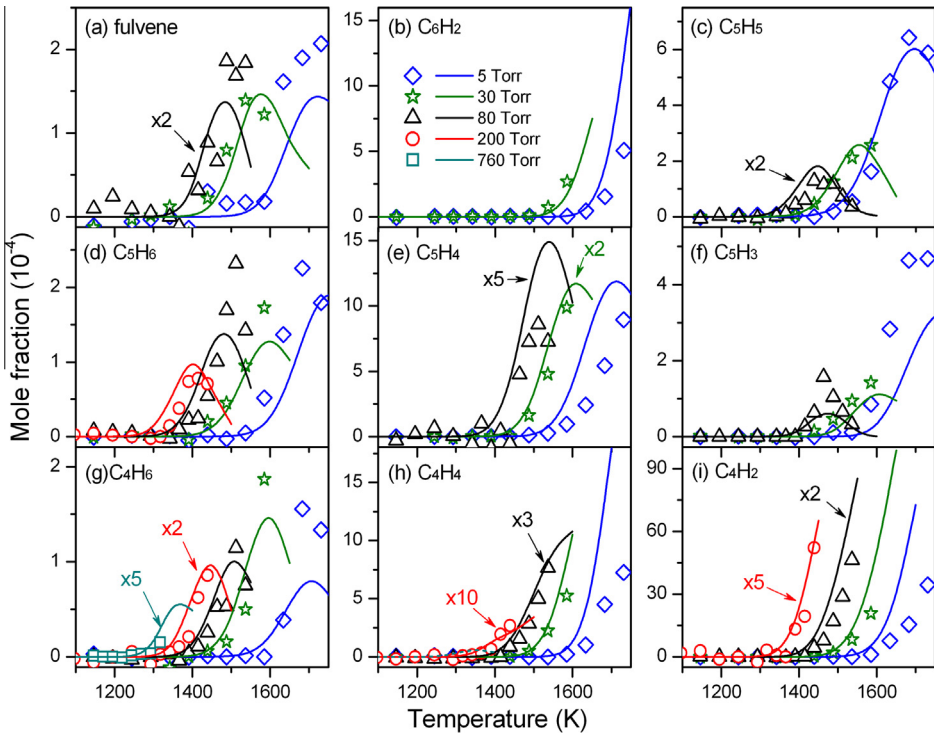


Fig. 2. Experimental (symbols) and simulated (lines) mole fraction profiles of fulvene, 1,3,5-hexatriyne (C_6H_2), cyclopentadienyl radical (C_5H_5), 1,3-cyclopentadiene (C_5H_6), pentatetraene (C_5H_4), pentatetraenyl radical (C_5H_3), 1,3-butadiene (C_4H_6), vinylacetylene (C_4H_4) and diacetylene (C_4H_2) in the flow reactor pyrolysis of toluene at different pressures.

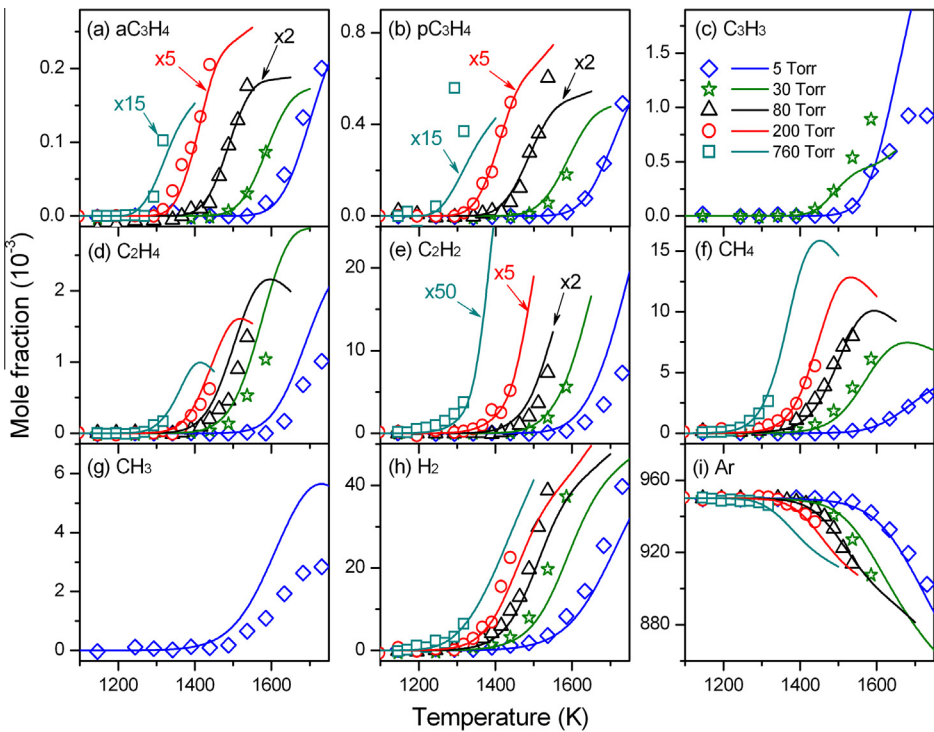


Fig. 3. Experimental (symbols) and simulated (lines) mole fraction profiles of allene (aC_3H_4), propyne (pC_3H_4), propargyl radical (C_3H_3), acetylene (C_2H_2), methane (CH_4), methyl radical (CH_3), hydrogen (H_2) and argon (Ar) in the flow reactor pyrolysis of toluene at different pressures.

other bonds in the $A1CH_3$ molecule [107], R1 dominates the unimolecular decomposition reactions of $A1CH_3$. For example, R1 and R2 contribute about 38% and 0.5% to the decomposition of $A1CH_3$ at 5 Torr and 1600 K, while at 760 Torr and 1350 K, R1 and R2 contribute about 13% and 2%.

The H-atom abstraction reactions of $A1CH_3$ mainly produce $A1CH_2$, which is consistent with previous modeling work of toluene pyrolysis and oxidation [6,10,11,24,26,27,31,32]. Among the H-atom abstraction reactions, those by H (R4), (R5) are the most dominant ones and contribute more than 40% to the

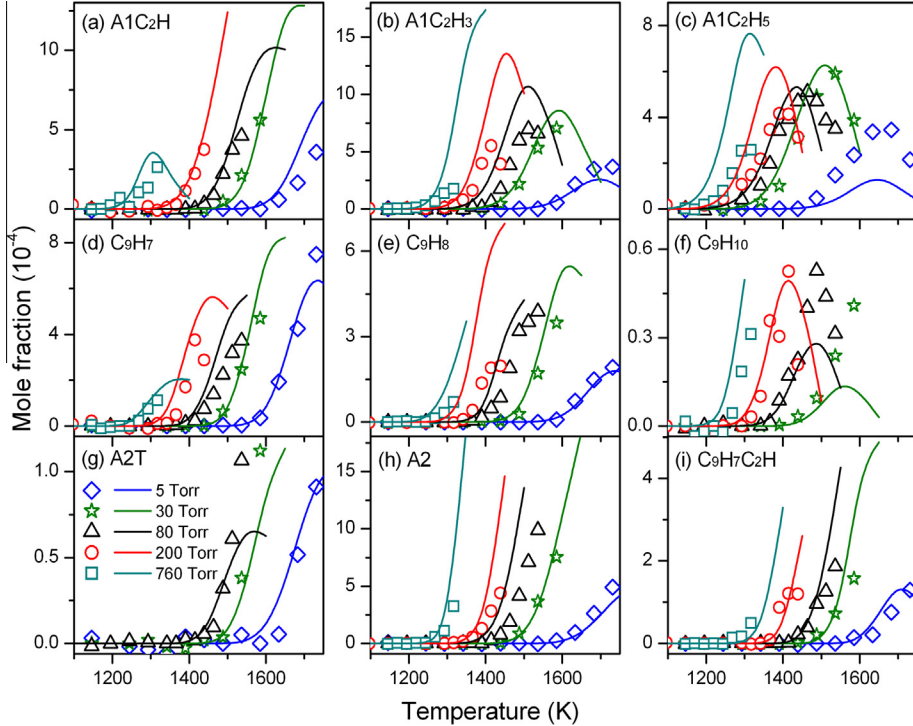


Fig. 4. Experimental (symbols) and simulated (lines) mole fraction profiles of phenylacetylene (A_1C_2H), styrene ($A_1C_2H_3$), ethylbenzene ($A_1C_2H_5$), indenyl radical (C_9H_7), indene (C_9H_8), indane (C_9H_{10}), naphthalene (A_2T), naphthalene (A_2) and ethynylindene ($C_9H_7C_2H$) in the flow reactor pyrolysis of toluene at different pressures.

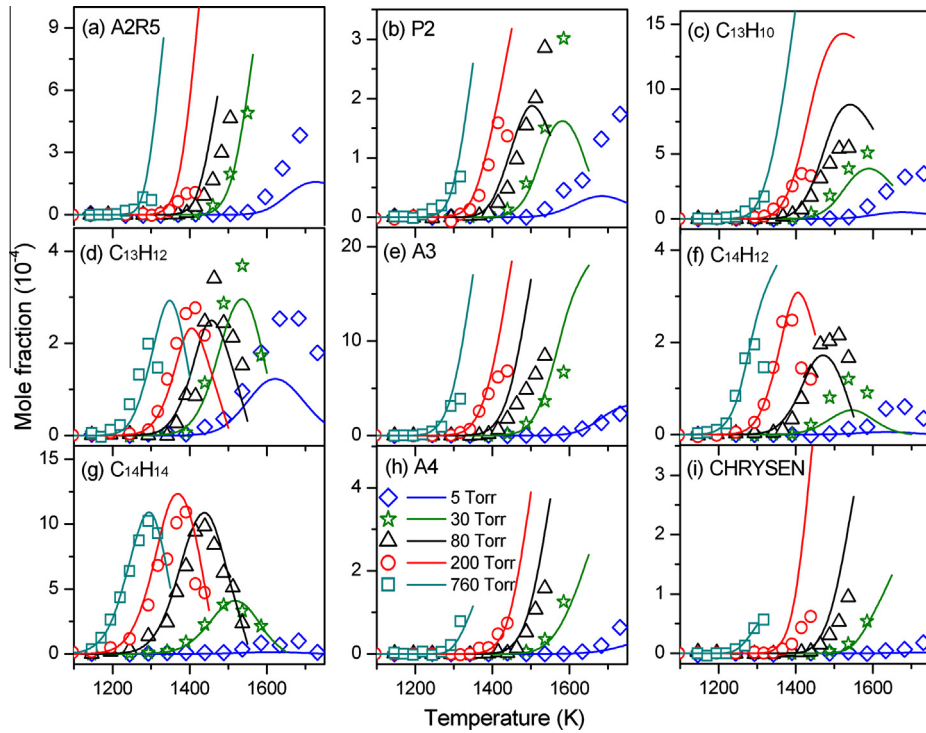


Fig. 5. Experimental (symbols) and simulated (lines) mole fraction profiles of acenaphthylene (A2R5), biphenyl (P2), fluorene ($C_{13}H_{10}$), diphenylmethane ($C_{13}H_{12}$), phenanthrene (A3), stilbene ($C_{14}H_{12}$), bibenzyl ($C_{14}H_{14}$), pyrene (A4) and chrysene (CHRYSEN) in the flow reactor pyrolysis of toluene at different pressures.

decomposition of A_1CH_3 in both the 5 and 760 Torr cases. Other important H-atom abstraction reactions include those by CH_3 , A_1^- and C_5H_5 radicals. Due to the dominant role of A_1CH_2 production in both unimolecular decomposition and H-atom abstraction of toluene, A_1CH_2 is formed with higher concentration levels than

other products in the early stage of toluene pyrolysis, as shown in Fig. 1. Besides A_1CH_2 , the unimolecular decomposition and H-atom abstraction reactions of A_1CH_3 can also produce $C_6H_4CH_3$. These pathways contribute about 2% together to the decomposition of A_1CH_3 in the 5 Torr case and about 6% in the 760 Torr case, and

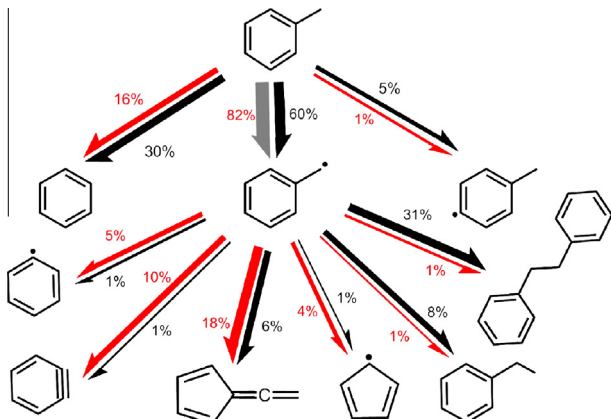


Fig. 6. Reaction network of toluene initial decomposition from the pyrolysis in flow reactor at 5 Torr, 1600 K and 760 Torr, 1350 K. The red and black arrows indicate the reaction fluxes at 5 and 760 Torr, respectively. The percentage in the figure means the carbon flux of the pathway divided by total carbon flux of toluene consumption.

are the main formation source of $C_6H_4CH_3$. Moreover, the ipso-substitution reaction R6 also plays an important role in the decomposition of $A1CH_3$ according to Fig. 7(b), and becomes the major source of A1 and CH_3 .

4.1.1.2. Decomposition of benzyl radical and other C_7 products. Benefiting from the application of SVUV-PIMS, $A1CH_2$ and its decomposition products C_7H_6 , $o\text{-}C_6H_4$ and C_5H_5 were unambiguously detected. Their experimental and simulated mole fraction profiles are presented in Figs. 1(b, c and f) and 2(c), respectively, which provide new experimental data for investigating the chemistry of $A1CH_2$. As seen from Fig. 1(b), the concentration level of $A1CH_2$ decreases as the pressure increases, and becomes too low to be detected in the 760 Torr case. The main consumption pathways of $A1CH_2$ change as the pressure increases. At low pressures, the unimolecular decomposition reactions (R17)–(R19) control the consumption of $A1CH_2$, while the self-combination of $A1CH_2$ and combination between $A1CH_2$ and small species have rising contributions as the pressure increases. These combination reactions are also important formation pathways of large MAHs and PAHs, and will be discussed in detail in Section 4.1.2. Recent theoretical studies [53,57,82] suggested that the pathway from $A1CH_2$ to $C_7H_6 + H$

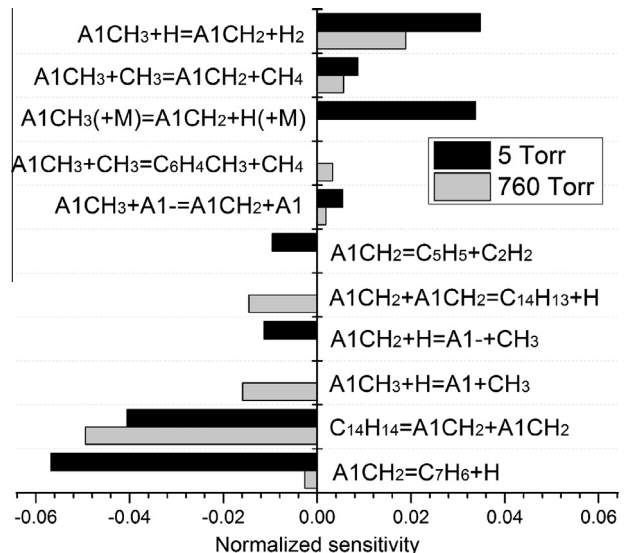


Fig. 8. Sensitivity analysis of benzyl ($A1CH_2$) from the pyrolysis of toluene in a flow reactor at 5 Torr, 1600 K and 760 Torr, 1350 K.

(R18) passes through multiple intermediates with fairly low energy barriers. The H atom has also been confirmed to be released from the benzene ring in the shock tube pyrolysis study reported by Sivaramakrishnan et al. [83]. Consequently, the ROP analysis indicates that R18 is the most important decomposition pathway of $A1CH_2$, and contributes almost 100% to the formation of C_7H_6 . The sensitivity analysis of $A1CH_2$ in Fig. 8 also demonstrates that in the 5 Torr case, R18 shows the largest sensitivity to the consumption of $A1CH_2$, while in the 760 Torr case, the self-combination of $A1CH_2$ shows the largest negative sensitivity. The experimental and simulated mole fraction profiles of C_7H_6 are shown in Fig. 1(c). It can be seen that the initial formation temperature of C_7H_6 is about 50 K higher than that of $A1CH_2$ at the same pressure, and its concentration level is very close to that of $A1CH_2$. Moreover, the other two important unimolecular decomposition pathways of $A1CH_2$ are R19 to produce $o\text{-}C_6H_4 + CH_3$ and R17 to produce $C_5H_5 + C_2H_2$. Figures 1(f) and 2(c) display the experimental and simulated mole fraction profiles of $o\text{-}C_6H_4$ and C_5H_5 , respectively. Both of them have similar formation temperatures to that of C_7H_6 .

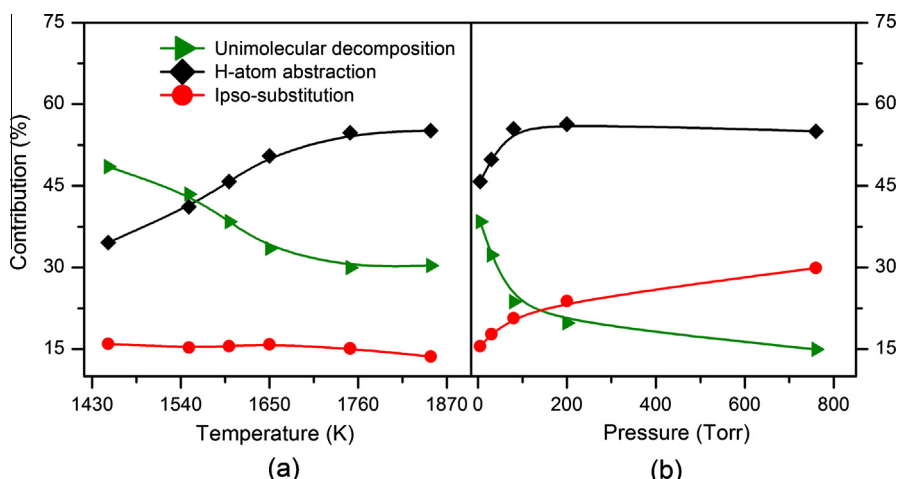


Fig. 7. The contributions of different reaction types to the consumption of toluene as the function of temperature at 5 Torr (a), and as the function of pressure at the same toluene conversion (50%) (b) according to the ROP analysis.

The main consumption pathways of C_7H_6 at all five pressures are to form C_7H_5 by unimolecular C–H fission (R25) or H-atom abstraction reactions. C_7H_6 can also suffer a minor decomposition pathway, that is, the unimolecular C–C fission to form $cC_5H_4 + C_2H_2$ (R26). C_7H_5 is almost totally formed from the decomposition of C_7H_6 . It is mainly consumed by unimolecular decomposition reactions and combination reactions at all five pressures. Its unimolecular decomposition will produce $C_4H_2 + C_3H_3$ (R28) and $C_5H_3 + C_2H_2$ (R29). Derudi et al. [57] performed theoretical investigation on the unimolecular decomposition of C_7H_5 and concluded that the former pathway is about an order of magnitude faster than the latter one at a wide pressure range from 0.013 to 10 bar. Consequently C_4H_2 and C_3H_3 become the dominant unimolecular decomposition products of C_7H_5 . This reaction also controls the formation of C_4H_2 and C_3H_3 at most pressures according to the ROP analysis. Besides, C_7H_5 can also suffer the self-combination reaction and combination reactions with C_3H_3 , C_5H_5 and $A1CH_2$ to produce PAHs, which will be discussed in Section 4.1.2.

4.1.1.3. Formation and consumption of C_6 and C_5 products. Figures 1(e and f) and 2(a–f) present the experimental and simulated mole fraction profiles of eight C_6 and C_5 products. A1 is another significant primary decomposition product of $A1CH_3$ besides $A1CH_2$. The ROP analysis shows that the ipso-substitution of $A1CH_3$ by H (R6) dominates the formation of A1 at all five pressures, and minor formation pathways of A1 include the H-atom abstraction of $A1CH_3$ by $A1^-$ and the isomerization reactions of fulvene. For fulvene, its frequently discussed formation pathways such as the self-combination of C_3H_3 and the combination reaction between C_3H_3 and aC_3H_5 were found to be inadequate for reproducing its concentration levels in this work. According to the theoretical investigation, Sharma and Green [108] found that the reaction sequence $C_5H_5 + CH_3 \rightarrow C_5H_4CH_3 \rightarrow$ fulvene plays an important role for fulvene formation, especially at high temperature region. Due to the easy production and high concentration levels of C_5H_5 and CH_3 in toluene combustion, this reaction sequence dominates the formation of fulvene and makes it possible to capture the measured concentration levels of fulvene.

As an abundant product during the pyrolysis of toluene, $o\text{-}C_6H_4$ is dominantly produced from the unimolecular decomposition of $A1CH_2$ through R19 at all five pressures. The unimolecular decomposition reactions of $C_6H_4CH_3$ and $A1^-$ can also produce $o\text{-}C_6H_4$, but only have minor contributions. The dominant consumption pathway of $o\text{-}C_6H_4$ in the low pressure cases such as 5 and 30 Torr is the unimolecular decomposition reaction to produce $C_4H_2 + C_2H_2$. The formation reactions of PAHs from $o\text{-}C_6H_4$ become more and more important as the pressure increases.

The C_5 chemistry is significant in the combustion of aromatic fuels, especially in the pyrolysis of toluene, due to the crucial role of C_5H_5 in both fuel decomposition and PAHs formation. The main source of C_5H_5 in the thermal decomposition of toluene is still in debating now, which could be either the unimolecular decomposition reaction of $A1CH_2$ (R17) or the bimolecular reaction between C_7H_6 and H. According to the recent theoretical progresses on the unimolecular decomposition of $A1CH_2$ [53,57], the pathway producing $C_7H_6 + H$ (R18) has the lowest maximum energy barrier (84.9 kcal/mol in both [53] and [57]). Meanwhile, the difference in energy barrier between R17 and R18 (~6.8 kcal/mol [53]) was only slightly greater than that between R19 and R18 (~6.5 kcal/mol [57]). Thus it may be argued that the rate constant of R17 is probably comparable to that of R19. Considering the great reaction flux from $A1CH_2$ and the considerable contribution of R19 in $A1CH_2$ decomposition, it is reasonable that the ROP analysis shows that most of C_5H_5 is produced by R17 instead of the reaction between C_7H_6 and H. Figure S1 shows the change of C_5H_5 concentration with multiplying and dividing the rate constant of R17 by a factor of 3,

which reveals the great sensitivity of R17 to C_5H_5 . One of the main consumption pathways of C_5H_5 is the reaction with CH_3 to form $C_5H_4CH_3$ which then converts to fulvene. Another important consumption pathway of C_5H_5 is the unimolecular decomposition reaction to produce $C_3H_3 + C_2H_2$, especially at low pressures. Moreover C_5H_5 can also suffer self-combination or react with other small products to produce PAHs.

4.1.1.4. Formation and consumption of C_4 and smaller products. Figures 2(g–i) and 3 illustrate the experimental and simulated mole fraction profiles of $C_0\text{--}C_4$ species. Almost all of 1,3-butadiene (C_4H_6) come from the reaction $CH_3 + C_5H_5 = C_4H_6 + C_2H_2$. The subsequent two step H-atom elimination reaction sequence of C_4H_6 is an important formation source of C_4H_4 . Besides, C_4H_4 can be also produced via the reaction between C_3H_2 and CH_3 . Three C_3 species allene (aC_3H_4), propyne (pC_3H_4) and C_3H_3 were detected in the experiment. The ROP analysis shows that at all pressures, aC_3H_4 is mainly produced by the decomposition of C_5H_4 and C_5H_6 and the H-atom addition reaction of C_3H_3 . pC_3H_4 is dominantly produced by the H-atom addition reaction of C_3H_3 and the reaction between C_2H_2 and CH_3 , and partly from the isomerization of aC_3H_4 . C_3H_3 is an important intermediate in the pyrolysis and oxidation of toluene, since it contributes significantly to the formation and growth of PAHs. Over half of C_3H_3 is produced from the decomposition of C_7H_5 (R28). Other formation pathways of C_3H_3 include the decomposition of C_5H_5 , fulvene and C_7H_6 . There are a variety of formation pathways of C_2H_2 under pyrolysis conditions, and most of C_2H_2 is produced via the decomposition of $A1CH_2$, C_5H_5 , $o\text{-}C_6H_4$ and C_7H_6 . Figure 3(f–h) illustrates the profiles of CH_4 , CH_3 and H_2 . H_2 and CH_4 are abundantly produced by the H-atom abstraction reactions of $A1CH_3$, C_7H_6 and A1, while CH_3 is mainly produced by the ipso-substitution reaction of $A1CH_3$ (R6) and the decomposition reactions of $A1CH_2$ (R19), (R20).

4.1.2. Aromatics growth

4.1.2.1. Growth of MAHs. Figures 4 and 5 present the experimental and simulated mole fraction profiles of some large MAHs and PAHs. The large MAHs observed in this experiment mainly include $A1C_2H$, $A1C_2H_3$ and $A1C_2H_5$. Their mole fraction profiles are shown in Fig. 4(a–c). These large MAHs mainly originate from the combination reactions between $C_5\text{--}C_7$ cyclic radicals and $C_1\text{--}C_3$ species. For example, nearly all of $A1C_2H_5$ is produced from the combination reaction between $A1CH_2$ and CH_3 in all five cases due to the abundantly production of the two radicals in the primary decomposition of toluene, especially via R1, R4 and R6. The subsequent decomposition of $A1C_2H_5$ mainly proceeds through H-atom abstraction and unimolecular decomposition reactions to produce C_8H_9 radicals. Particularly, 1-phenylethyl radical ($A1CHCH_3$) affords more than three fifth reaction fluxes from $A1C_2H_5$, and can quickly decompose to $A1C_2H_3$ through the $\beta\text{-}C\text{-}H$ scission reaction which is also the most important formation pathway of $A1C_2H_3$ at all investigated pressures. There are also some minor formation pathways of $A1C_2H_3$, e.g. the combination reaction between C_5H_5 and C_3H_3 (R30) in the 5 Torr case and the decomposition of $C_{14}H_{12}$ in the 760 Torr case. The decomposition of $A1C_2H_3$ proceeds principally through the H-atom abstraction reactions to produce two C_8H_7 radicals ($A1CCH_2$ and $A1CHCH$) and the H-atom attack reactions to produce $A1 + C_2H_3$ and $A1^- + C_2H_4$. Further $\beta\text{-}C\text{-}H$ scission reactions of the two C_8H_7 radicals control the formation of $A1C_2H$ in the 760 Torr case, while the reactions between $A1^-$ and C_2H_2/C_2H become dominant in the 5 Torr case instead. $A1C_2H$ has a highly unsaturated molecular structure, making it quite easy to react with other species to generate PAHs.

4.1.2.2. Formation of bicyclic PAHs. In this work, a number of bicyclic PAHs were observed. Their experimental and simulated mole

fraction profiles are mainly presented in Figs. 4 and 5. The discussion will be focused on C₉H₈ and A2 which are generally the most important bicyclic PAHs in combustion.

C₉H₈ is composed of a benzene ring fused with a five-member ring, and has a number of possible formation pathways such as A1CH₂ + C₂H₂ (R31), C₆ species + C₃ species, C₅H₆ + C₅H₅ (R32) and C₇H₆ + C₂H₂. Vereecken and Peeters [92,93] investigated the reactions of A1CH₂ + C₂H₂ and C₆ species + C₃ species theoretically. They concluded that the formation of C₉H₈ + H dominates the reactions of A1CH₂ + C₂H₂, but has almost no contribution or less than 5% contribution in the reactions of A1 – + C₃H₄ isomers. Due to the abundant production of A1CH₂ and C₂H₂ in toluene pyrolysis, R31 controls the formation of C₉H₈ at all investigated pressures, while the other formation pathways only have very limited contributions. The consumption of C₉H₈ mainly produces C₉H₇ through H-atom abstraction and unimolecular decomposition reactions. C₉H₇ is the largest radical observed in this experiment, and its concentration levels are also relatively high, implying its important role in the growth process of PAHs. The main formation pathways of C₉H₇ change as the pressure decreases. Most of C₉H₇ is formed from the H-atom abstraction reaction of C₉H₈ in the 760 Torr case, while at 5 Torr, it is mainly formed through the reactions of A1 – + C₃H₃, o-C₆H₄ + C₃H₃ and C₅H₅ + C₄H₂. For the other two observed species with a benzene ring fused with a five-member ring in Fig. 4(f and i), indane (C₉H₁₀) is mainly produced from the reaction between A1CH₂ and C₂H₄, while most of ethynylindene (C₉H₇C₂H) is formed from the reaction between C₇H₅ and C₄H₃ radicals.

As seen from Fig. 4, A2 has the highest concentration levels among all observed bicyclic PAHs at most investigated pressures. The formation mechanism of A2 is very complicated and includes a great deal of possible pathways. These pathways can be divided into several types, such as C₅ + C₅ [98,109], C₆ + C₄ [96,110], C₇ + C₃ [6,8,76], C₈ + C₂ [6,76] and C₉ + C₁ [8,91], and were all included in this model. The ROP analysis shows that at all investigated pressures, A2 mainly comes from the unimolecular decomposition reaction (R33) of C₉H₇CH₂ which is produced through the reactions of C₉H₇ + CH₃ and A1CH₂ + C₃H₃. Besides, the subsequent decomposition of C₉H₇CH₂ can also lead to C₉H₆CH₂ which can isomerize to A2 (R34). The other important formation pathways of A2 include the self-combination of C₅H₅ via C₅H₅–C₅H₄ (R35), (R36) and the combination of C₇H₅ + C₃H₃ (R37).

Besides the fused bicyclic PAHs, some unfused bicyclic PAHs were also observed in this experiment, including P2, C₁₃H₁₂, C₁₄H₁₂ and C₁₄H₁₄, as shown in Fig. 5. These aromatics mainly originate from the reactions of C₆–C₇ MAHs + C₆–C₇ MAHs. For example, it is widely accepted that P2 is the product of the self-combination of A1 – and reaction between A1 and A1 –. In a recent experimental and theoretical investigation, Shukla et al. [101] concluded that P2 is the most preferred product of these reactions. Consequently the self-combination of A1 – becomes the most important formation pathway of P2 in the 5 Torr case, while the reaction between A1 and A1 – replaces the dominant role in the 760 Torr case. The dominant formation pathways of C₁₃H₁₂ and C₁₄H₁₄ in all five cases are the combination reaction between A1 – and A1CH₂ and the self-combination reaction of A1CH₂, respectively. C₁₄H₁₂ is mainly formed from the unimolecular decomposition of C₁₄H₁₃ radical, while C₁₄H₁₃ can be produced from the decomposition of C₁₄H₁₄ and the other self-combination reaction of A1CH₂. It has been mentioned in Section 4.1.1.2 that the contribution of self-combination in the consumption of A1CH₂ rapidly raises as the pressure increases. Consequently in the high pressure cases such as 200 and 760 Torr, A1CH₂ self-combination becomes the most important consumption pathway of A1CH₂, and the simulated results of C₁₄H₁₄ is very sensitive to the major formation pathway of A1CH₂ (R4) according to the sensitivity analysis of C₁₄H₁₄ in Fig. 10.

Therefore the reproduction of measured C₁₄H₁₄ and C₁₄H₁₂ profiles by this model at these pressures also provides validation for benzyl chemistry.

4.1.2.3. Formation of tricyclic and tetracyclic PAHs. In this work, several tricyclic and tetracyclic PAHs were detected, such as A2R5, C₁₃H₁₀, A3, A4 and chrysene. Their experimental and simulated mole fraction profiles are presented in Fig. 5. It is well known that A2R5 can be produced from the addition of C₃H₃ on C₉H₇ (R39), which is also the dominant formation pathway of A2R5 in this work except for the 5 Torr case. Shukla et al. [101] suggested that A2R5 can also be produced from the unimolecular decomposition of the radical of biphenyl (P2 –). By using their calculated result in this model, it is concluded that the reaction P2 – = A2R5 + H only becomes significant in the 5 Torr case. For C₁₃H₁₀, it is mainly formed from the reaction sequence C₁₃H₁₂ → C₁₃H₁₁ → C₁₃H₁₀ and decomposes to C₁₃H₉.

As a typical tricyclic PAH, A3 has similar concentration levels to A2 at all investigated pressures. The ROP analysis shows that the dominant formation pathways of A3 are very different as the pressure changes. In the 760 Torr case, the decomposition reaction sequence C₁₄H₁₂ → stilbenyl radical (C₁₄H₁₁) → A3, which has been theoretically investigated by Matsugi and Miyoshi [8], controls the formation of A3 due to the high concentration levels of C₁₄ bicyclic PAHs. In the 5 Torr case, the self-combination reaction of C₇H₅ (R40) is the most important pathway. Besides, other important formation pathways of A3 include the bimolecular reactions of C₉H₇ + C₅H₅ and A1 – + A1C₂H and the unimolecular decomposition of C₁₃H₉CH₂ (R41) which is mainly produced from the reaction of A1CH₂ + C₇H₅.

Two tetracyclic PAHs A4 and chrysene were detected in this work, as shown in Fig. 5(h and i). The ROP analysis shows that the reaction between C₁₃H₉ and C₃H₃ is the dominant formation source for A4 in the 5 Torr case. In the 760 Torr case, the situation is slightly different. The reaction of A3–4 + C₂H₂ becomes slightly more important than the reaction of C₁₃H₉ + C₃H₃. For chrysene, it is almost totally formed from the self-combination reaction of C₉H₇ in all cases.

According to the discussion above, it can be summarized that C₇ radicals including A1CH₂ and C₇H₅ play important roles in the formation of PAHs, which reveals the fuel-specific formation pathways of PAHs in toluene pyrolysis. Based on the ROP analysis, the reaction networks from A1CH₂ to PAHs at 5 and 760 Torr were drawn in Fig. 9. It is noteworthy that the formation pathways of PAHs, especially those with three and more fused rings are still not very clear now. Further experimental and theoretical efforts are needed to understand the growth mechanism of large PAHs more clearly.

4.1.3. Comparison with previous toluene models

The toluene models of Metcalfe et al. [29] (referred as the Metcalfe model) and Narayanaswamy et al. [7] (referred as the Narayanaswamy model) were used to simulate the pyrolysis of toluene at 760 Torr in comparison with the present model. The comparisons of experimental and simulated results using the three models are illustrated in Fig. 11. Both the present model and the Narayanaswamy model can capture the decomposition of toluene, while the Metcalfe model over-predicts the reactivity of toluene. The three models can also predict the formation of H₂, CH₄ and A1C₂H₅ within the experimental uncertainties. The Narayanaswamy model under-predicts the formation of C₂H₄ and A1C₂H₃. It should be noted that there is no PAHs sub-mechanism in the Metcalfe model, while the Narayanaswamy model did not include the self-combination reactions of A1CH₂. Thus these species were not compared.

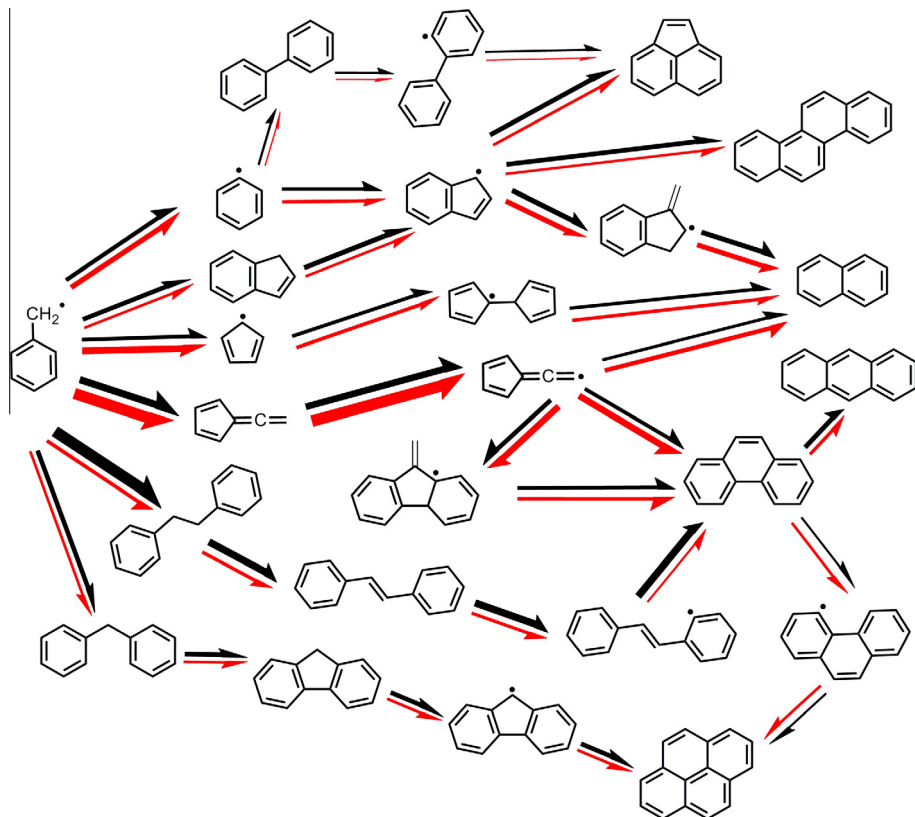


Fig. 9. The reaction network from benzyl radical to PAHs at 5 Torr, 1600 K and 760 Torr, 1350 K. The red and black arrows indicate the reaction fluxes from the pyrolysis of toluene in a flow reactor at 5 and 760 Torr, respectively.

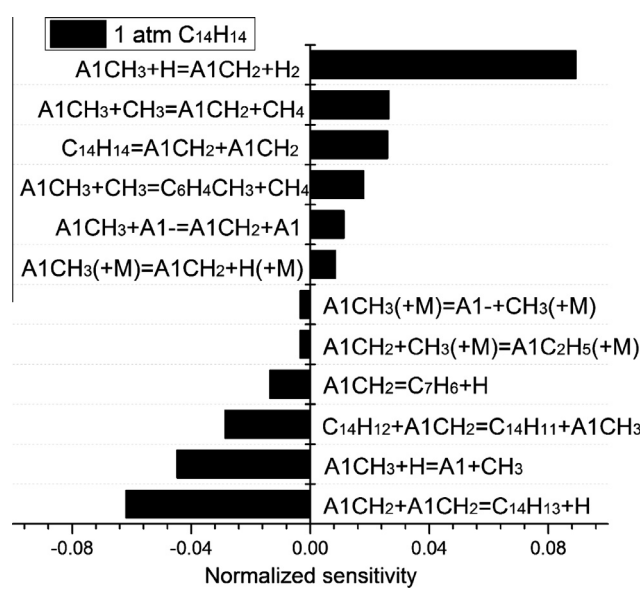


Fig. 10. Sensitivity analysis of bibenzyl ($C_{14}H_{14}$) in the flow reactor pyrolysis of toluene at 760 Torr and 1350 K.

For the comparison of the 30 Torr simulation, the Metcalfe model can be used since pressure-dependent rate constants were considered for some key reactions. The model of Matsugi and Miyoshi [8] (referred as the Matsugi model) can also be used since it was developed for low pressure pyrolysis of toluene. The comparisons of experimental and simulated results are illustrated in Figs. S2 and S3 in Supplementary Materials. All three models can

well capture the decomposition of toluene at 30 Torr. Both the present model and the Matsugi model can predict the formation of CH_4 , C_2H_2 , $A1$, C_7H_5 , C_7H_6 , $A1C_2H_3$ and $A3$ within the experimental uncertainties. However, the Matsugi model predicts the formation of some important PAHs such as C_9H_8 and $A2$ towards high temperature region, and also over-predicts the concentrations of $C_{14}H_{14}$. Besides, the Metcalfe model over-predicts the concentrations of C_5H_5 , C_5H_6 and C_2H_2 , and under-predicts the concentrations of CH_4 , C_2H_4 and $A1C_2H_3$.

4.2. Jet stirred reactor oxidation

In this work, the JSR oxidation of toluene was performed at 10 atm with $\phi = 0.5$, 1.0 and 1.5. The detailed experimental conditions are listed in Table 1. The simulation was performed with the Perfectly Stirred Reactor module in the Chemkin-Pro software [106]. To validate the model against oxidation data at various pressures, the previous JSR oxidation data of toluene at 1 atm with $\phi = 0.5$, 1.0 and 1.5 [24] were also simulated. The experimental and simulated results are shown in Figs. 12–17. Generally this model shows satisfactory performance in capturing the formation temperatures and maximum mole fractions for most species. The ROP analysis was performed to reveal the reaction networks in both the 1 and 10 atm oxidation of toluene. For the 10 atm oxidation, the ROP analysis was performed at 1000 K for $\phi = 0.5$, 1050 K for $\phi = 1.0$ and 1100 K for $\phi = 1.5$, where most of products reach their peak mole fractions and nearly half of toluene is consumed. For the 1 atm oxidation, the analysis was performed at 1200 K, 1300 K and 1350 K, respectively. The reaction networks at $\phi = 1.0$ are shown in Fig. 18 as an example. Since the thermal decomposition reactions have been discussed in detail in last section, the discussion in this section will be focused on the oxidation reactions.

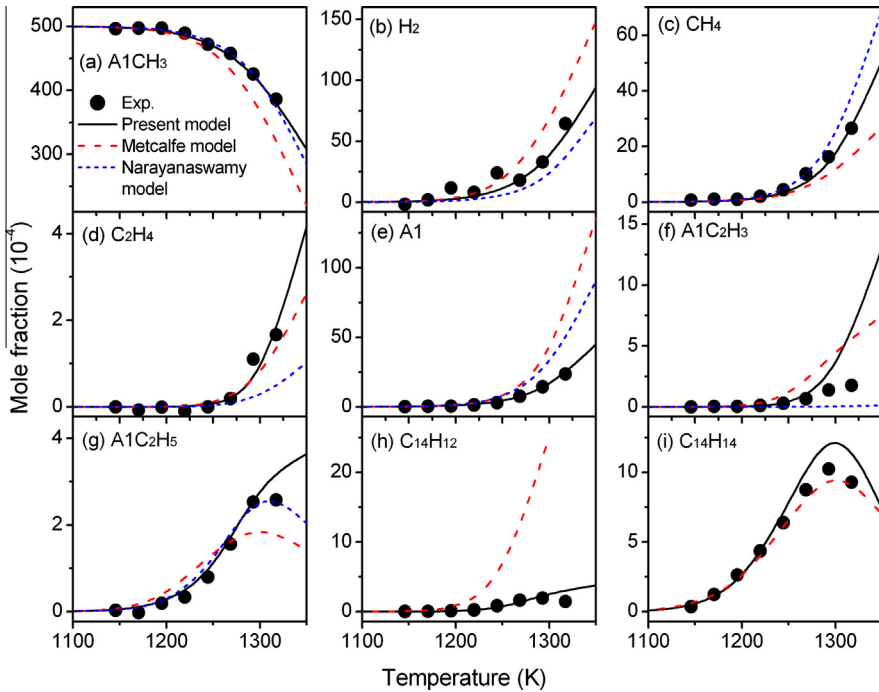


Fig. 11. Experimental (symbols) and simulated (lines) mole fractions of toluene ($A1CH_3$), hydrogen (H_2), methane (CH_4), ethylene (C_2H_4), benzene ($A1$), styrene ($A1C_2H_3$), ethylbenzene ($A1C_2H_5$), stilbene ($C_{14}H_{12}$) and bibenzyl ($C_{14}H_{14}$) in the flow reactor pyrolysis of toluene at 760 Torr using the present model, Metcalfe model [29] and Narayanaswamy model [7].

Table 1
Toluene JSR oxidation: experimental conditions.

ϕ	T (K)	P (atm)	τ (s)	Dilution (% mole)	References
0.5	1000–1300	1.0	0.07	0.15	[24]
1.0	1100–1350	1.0	0.10	0.15	[24]
1.5	1100–1400	1.0	0.12	0.15	[24]
0.5	950–1200	10.0	0.60	0.10	This work
1.0	950–1200	10.0	0.60	0.10	This work
1.5	950–1200	10.0	0.60	0.10	This work

Figures 12 and 13 illustrate the experimental and simulated mole fraction profiles of oxidation species at both 1 and 10 atm with $\phi = 1.5$. At both pressures, $A1CH_3$ is mainly consumed by the H-atom abstraction reactions by H (R4), OH (R7) and O (R11) to produce $A1CH_2$, but the dominant consumption pathway is different. At 1 atm, R4 is the most important consumption pathway of toluene with a contribution of about 43%, while at 10 atm, R7 becomes more important with a contribution of about 35%. According to both the ROP analysis and the sensitivity analysis, this difference between 1 and 10 atm can attribute to the lower temperature at 10 atm. The ROP analysis indicates that a large amount of HO_2 is formed from the oxidation reaction of H (R42), HCO (R43), cyclopentadienol-1-yl radical (C_5H_4OH , R44) and $C_5H_4CH_3$ (R45) at 10 atm, among which R42 is the dominant reaction. The formed HO_2 then converts to OH through the reaction $A1CH_2 + HO_2 = A1CH_2O + OH$ (R21). The sensitivity analysis of toluene at $\phi = 1.5$ and pressures of 1 and 10 atm in Fig. 19 also indicates that R21 has the largest negative sensitivity to toluene at 10 atm. The other important consumption pathways of $A1CH_3$ include the ipso-substitution by H (R6), the H-atom abstraction by OH to produce $C_6H_4CH_3$ (R8) and the reactions between $A1CH_3$ and O to produce $OC_6H_4CH_3$ (R13) and $HOOC_6H_4CH_3$ (R14). Similarly, the main consumption pathways of O₂ are also different between 1 and 10 atm. At 1 atm, the reaction $H + O_2 = O + OH$ dominates the consumption of O₂, while at 10 atm, most of O₂ reacts with H to produce HO_2 (R42).



At 1 atm, most of $A1CH_2$ is consumed by the reverse reaction of R1 to produce $A1CH_3$ and the isomerization reaction to produce $C_6H_4CH_3$, and only less than 20% is oxidized by O to produce $A1CH_2O$. At 10 atm, the oxidation reaction by O becomes the dominant consumption pathway of $A1CH_2$, and more than one third of $A1CH_2$ is oxidized by HO_2 to produce $A1CH_2O$ and OH (R21). As introduced in Section 3.1.3, $A1CH_2O$ has three important decomposition pathways, i.e. $A1CHO + H$, $A1 + HCO$ and $A1 - + CH_2O$. According to the ROP analysis, the first one is more preferred at both pressures, and is also the dominant formation pathway of $A1CHO$. The experimental and simulated mole fraction profiles of $A1CHO$ are presented in Fig. 13(i). It can be seen that the maximum mole fraction of $A1CHO$ at 10 atm is larger than that at 1 atm, which is in accordance with the increasing contribution of oxidation reactions in the consumption of $A1CH_2$ as the pressure increases.

The role of $C_6H_4CH_3$ in the JSR oxidation is more important than that in the flow reactor pyrolysis. It is mainly formed from the benzenoid H-atom abstraction reaction of $A1CH_3$ at 10 atm, and becomes one of the most important consumption products of $A1CH_2$ at 1 atm. It is mainly consumed by the reactions with O₂ to produce *ortho*-benzoquinone (*o*- $C_6H_4O_2$) + CH_3 and $OC_6H_4CH_3 + O$ (R23). The former reaction is slightly more preferred at both pressures, and is also the dominant formation pathway of *o*- $C_6H_4O_2$. Besides, the reaction between $A1 -$ and O₂ (R33) is the second important formation pathway of *o*- $C_6H_4O_2$. The decomposition of *o*- $C_6H_4O_2$ can easily proceed through the CO elimination reaction to produce 2,4-cyclopentadiene-1-one (C_5H_4O) which then decomposes to $C_4H_4 + CO$. Figure 13(c) presents the experimental and simulated mole fraction profiles of C_4H_4 . The maximum mole fraction of C_4H_4 at 1 atm is about 5 times high as that

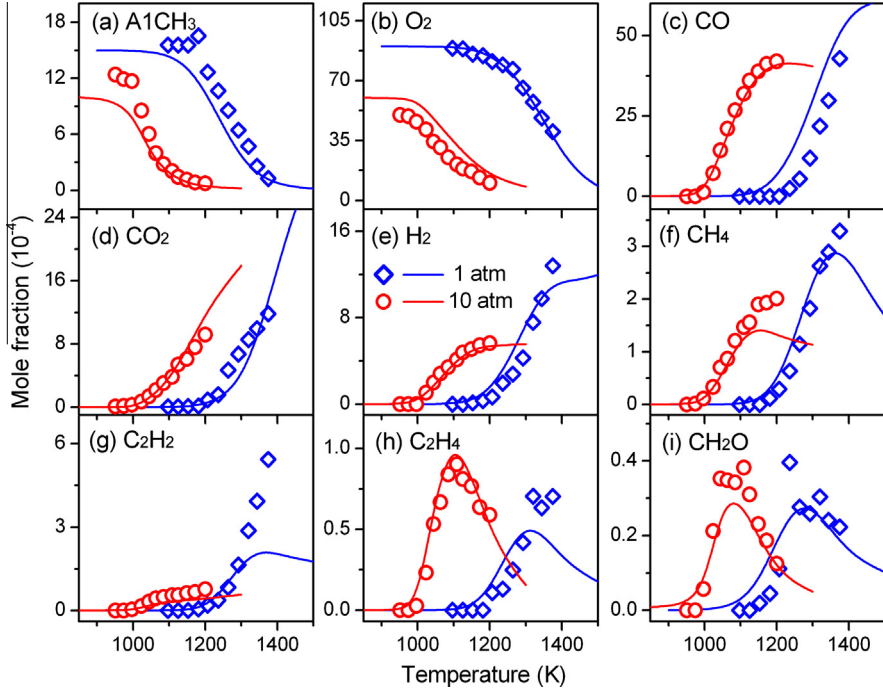


Fig. 12. Experimental (symbols) and simulated (lines) mole fraction profiles of toluene ($\text{A}1\text{CH}_3$), oxygen (O_2), carbon monoxide (CO), carbon dioxide (CO_2), hydrogen (H_2), methane (CH_4), acetylene (C_2H_2), ethylene (C_2H_4) and formaldehyde (CH_2O) in the JSR oxidation of toluene at 1 atm [24] and 10 atm with the equivalence ratio of 1.5.

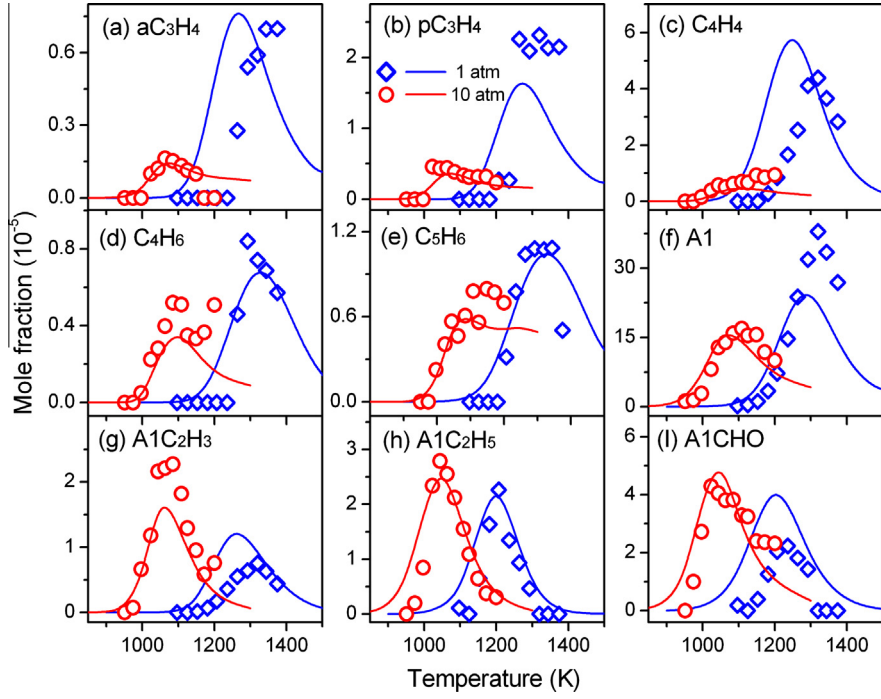


Fig. 13. Experimental (symbols) and simulated (lines) mole fraction profiles of allene (aC_3H_4), propyne (pC_3H_4), vinylacetylene (C_4H_4), 1,3-butadiene (C_4H_6), 1,3-cyclopentadiene (C_5H_6), benzene ($\text{A}1$), styrene ($\text{A}1\text{C}_2\text{H}_3$), ethylbenzene ($\text{A}1\text{C}_2\text{H}_5$) and benzaldehyde ($\text{A}1\text{CHO}$) in the JSR oxidation of toluene at 1 atm [24] and 10 atm with the equivalence ratio of 1.5.

at 10 atm, which can be explained by the abundant production of $\text{C}_6\text{H}_4\text{CH}_3$ via the isomerization of $\text{A}1\text{CH}_2$ at 1 atm.

$\text{OC}_6\text{H}_4\text{CH}_3$ is also mainly formed from R23 at both pressures, and is almost totally converted to $\text{C}_5\text{H}_4\text{CH}_3$ and CO (R24). The consumption of $\text{C}_5\text{H}_4\text{CH}_3$ through the reaction sequence $\text{C}_5\text{H}_4\text{CH}_3 \rightarrow \text{fulvene} (\rightarrow \text{C}_5\text{H}_5\text{CH}_2) \rightarrow \text{A}1$ can lead to the production

of A1. Figure 13(f) presents the experimental and simulated mole fraction profiles of A1. The other key formation pathway of A1 at both pressures is the ipso-substitution reaction of $\text{A}1\text{CH}_2$ by H (R6). Besides, the decomposition reaction of $\text{A}1\text{CH}_2\text{O}$ to produce $\text{A}1 + \text{HCO}$ is also an important formation pathway of A1 at 10 atm. The consumption of A1 mainly produces $\text{A}1^-$, $\text{A}1\text{O}$ and

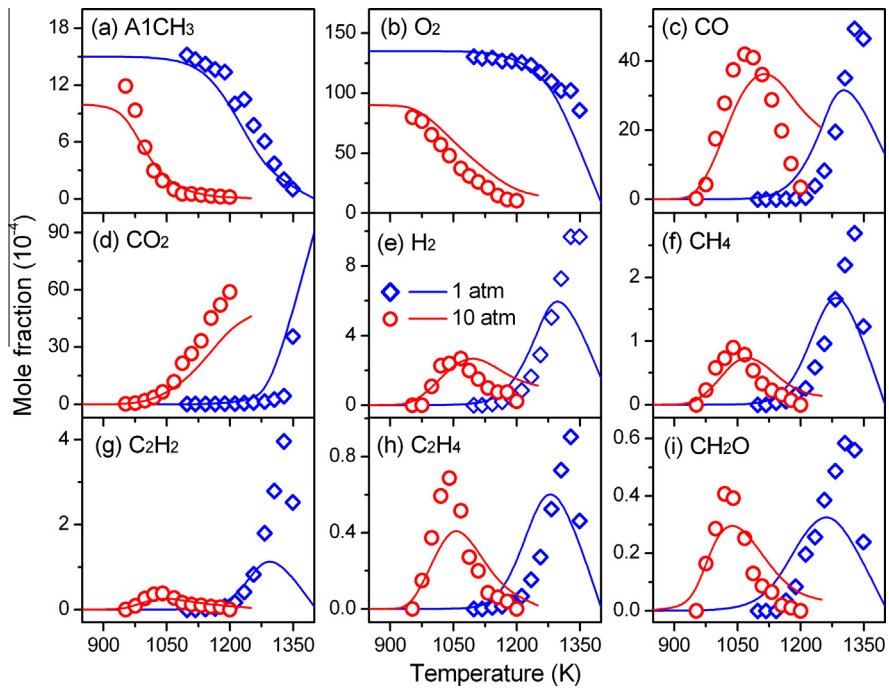


Fig. 14. Experimental (symbols) and simulated (lines) mole fraction profiles of toluene (A1CH₃), oxygen (O₂), carbon monoxide (CO), carbon dioxide (CO₂), hydrogen (H₂), methane (CH₄), acetylene (C₂H₂), ethylene (C₂H₄) and formaldehyde (CH₂O) in the JSR oxidation of toluene at 1 atm [24] and 10 atm with the equivalence ratio of 1.0.

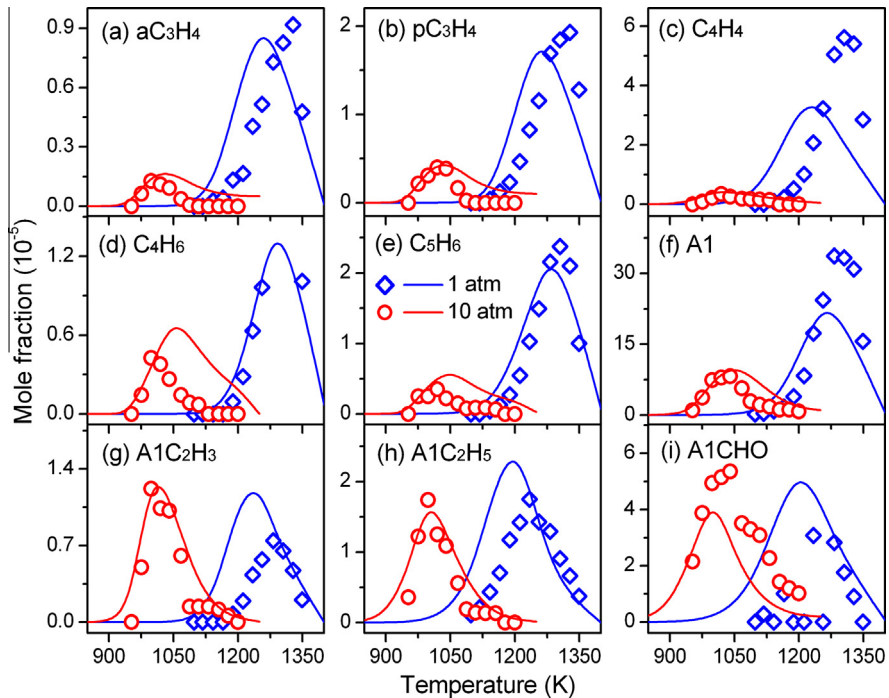


Fig. 15. Experimental (symbols) and simulated (lines) mole fraction profiles of allene (aC₃H₄), propyne (pC₃H₄), vinylacetylene (C₄H₄), 1,3-butadiene (C₄H₆), 1,3-cyclopentadiene (C₅H₆), benzene (A1), styrene (A1C₂H₃), ethylbenzene (A1C₂H₅) and benzaldehyde (A1CHO) in the JSR oxidation of toluene at 1 atm [24] and 10 atm with the equivalence ratio of 1.0.

A1OH, and the further oxidation reactions of A1— will also lead to the production of A1O. The subsequent decomposition of A1O mainly produces C₅H₅ + CO, and the reaction of C₅H₅ with H can lead to the production of C₅H₆. The decomposition and oxidation reactions of A1OH are the other source of C₅H₆. Figure 13(e) presents the experimental and simulated mole fraction profiles of C₅H₆.

Another consumption pathway of A1CH₂ is to produce A1C₂H₅ by the combination reaction with CH₃. This pathway is much more significant at 10 atm, and contributes almost 30% to the consumption of A1CH₂. Similar to the situations in the pyrolysis, further decomposition of A1C₂H₅ also follows the reaction sequence A1C₂H₅ → A1CHCH₃/A1CH₂CH₂ → A1C₂H₃. Figure 13(g and h) presents the mole fraction profiles of A1C₂H₃ and A1C₂H₅. Both

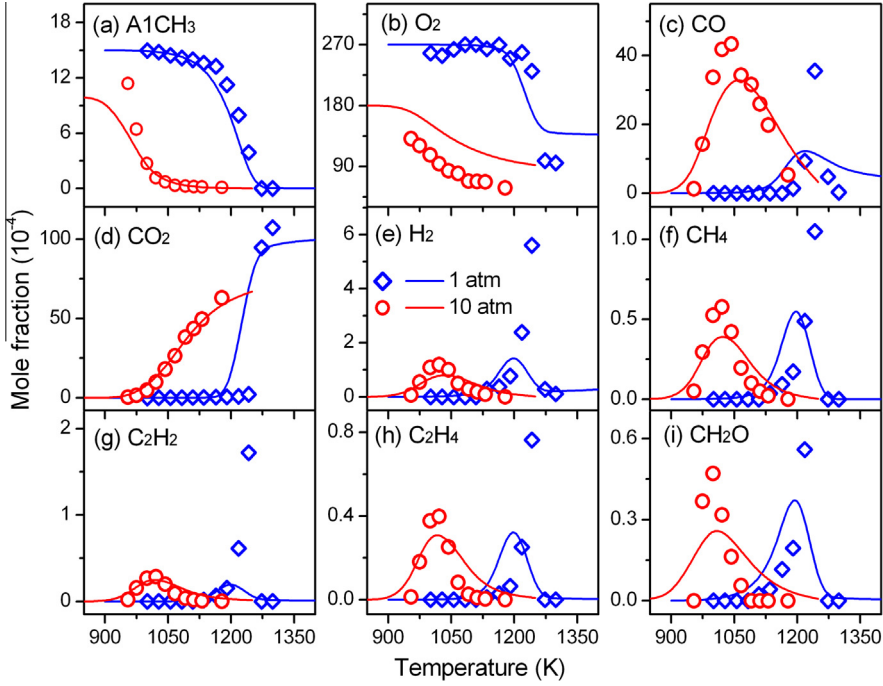


Fig. 16. Experimental (symbols) and simulated (lines) mole fraction profiles of toluene (A1CH₃), oxygen (O₂), carbon monoxide (CO), carbon dioxide (CO₂), hydrogen (H₂), methane (CH₄), acetylene (C₂H₂), ethylene (C₂H₄) and formaldehyde (CH₂O) in the JSR oxidation of toluene at 1 atm [24] and 10 atm with the equivalence ratio of 0.5.

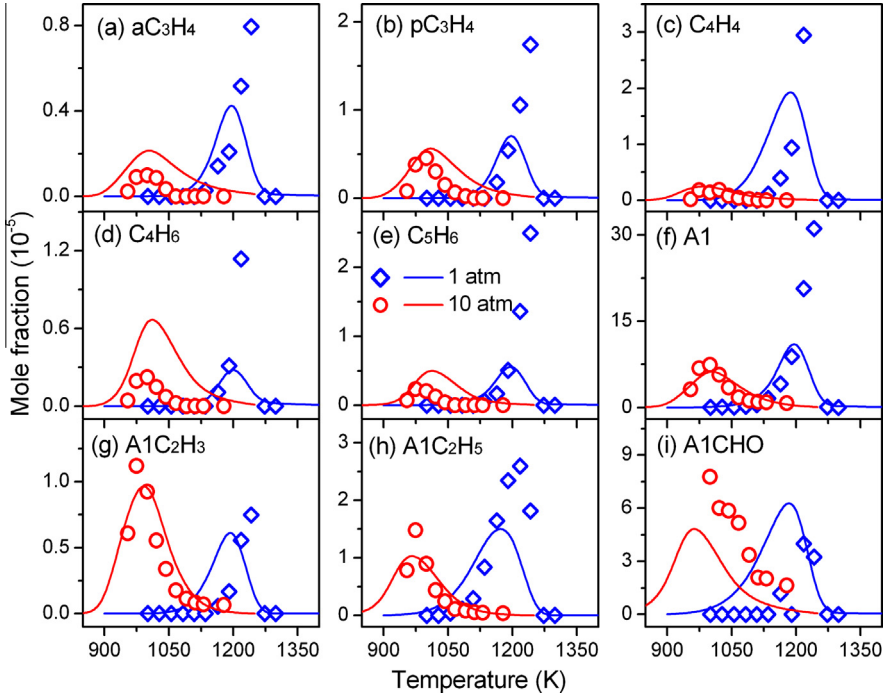


Fig. 17. Experimental (symbols) and simulated (lines) mole fraction profiles allene (aC₃H₄), propyne (pC₃H₄), vinylacetylene (C₄H₄), 1,3-butadiene (C₄H₆), 1,3-cyclopentadiene (C₅H₆), benzene (A1), styrene (A1C₂H₃), ethylbenzene (A1C₂H₅) and benzaldehyde (A1CHO) in the JSR oxidation of toluene at 1 atm [24] and 10 atm with the equivalence ratio of 0.5.

experimental and simulated maximum mole fractions of A1C₂H₃ and A1C₂H₅ at 10 atm are slight higher than those at 1 atm.

Figure 12(c–i) presents the experimental and simulated mole fraction profiles of hydrogen and some C₁–C₂ products. For some species among them, the main formation pathways at 1 and 10 atm are quite different. For example, it can be seen from

Fig. 12(g) that the maximum mole fraction of C₂H₂ at 1 atm is much higher than that at 10 atm. The ROP analysis shows that C₂H₂ is mainly produced from the decomposition of pC₃H₄ and C₂H₃ at 1 atm; however most of C₂H₃ participates in the oxidation reactions with O₂ to produce CH₂CHO or CH₂O at 10 atm, rather than decomposes to C₂H₂.

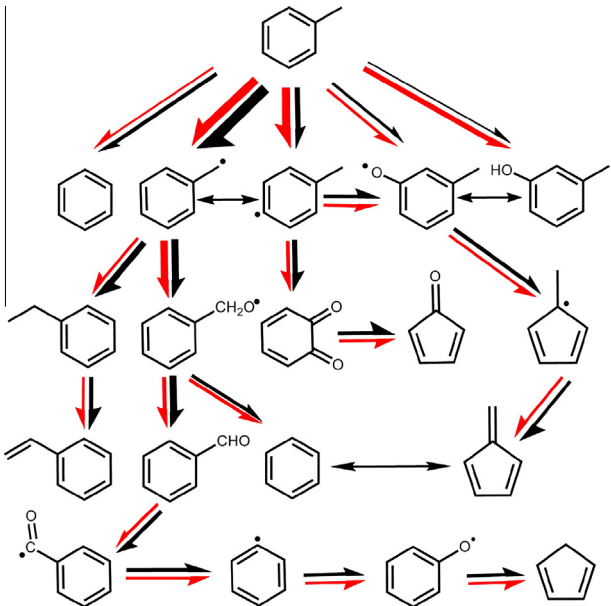


Fig. 18. The reaction network in the JSR oxidation of toluene at $\phi = 1.0$. The red and black arrows indicate the reaction fluxes at 1 and 10 atm, respectively.

Figures 14 and 15 illustrate the experimental and simulated mole fraction profiles of oxidation species at 1 and 10 atm with $\phi = 1.0$. Despite the slightly increasing contributions of oxidation reactions, the major reaction network is very similar to that in the $\phi = 1.5$ oxidation, and will not be discussed here. The major reaction networks at 1 and 10 atm with $\phi = 1.0$ are shown in Fig. 18. It can be seen that the oxidation pathways of A1CH_3 at these two pressures are quite similar, and A1CH_2 and $\text{C}_6\text{H}_4\text{CH}_3$ afford the greatest reaction fluxes from A1CH_3 at both pressures. At 10 atm, A1 is more preferred to be formed directly from the decomposition of A1CH_3 , while at 1 atm $\text{HOCH}_2\text{C}_6\text{H}_4\text{CH}_3$ is more favored to be produced than that at 10 atm. The consumption of A1CH_2 at these two pressures produced both combination products and oxidation products. At 10 atm, more $\text{A1C}_2\text{H}_5$ is formed from the reaction between A1CH_2 and CH_3 , while at 1 atm the formation of the oxidation product $\text{A1CH}_2\text{O}$ is more competitive.

Figures 16 and 17 present the experimental and simulated mole fraction profiles of oxidation species at both 1 and 10 atm with ϕ

= 0.5. Compared to the fuel-rich condition, the contributions of H-atom abstraction reactions by OH and O to the consumption of A1CH_3 increase obviously, as indicated by the ROP analysis. The H-atom abstraction reactions by O contribute about 15% to the consumption of A1CH_3 at 1 and 10 atm. The formed A1CH_2 mainly reacts with HO_2 and O to produce $\text{A1CH}_2\text{O}$. The major formation and oxidation pathways of $\text{C}_6\text{H}_4\text{CH}_3$ are similar to those at the rich condition. Especially, $\text{C}_6\text{H}_4\text{CH}_3$ can still react with O₂ and HO₂ to produce $\text{o-C}_6\text{H}_4\text{O}_2$ and $\text{OC}_6\text{H}_4\text{CH}_3$. The subsequent decomposition pathways of $\text{A1CH}_2\text{O}$ and $\text{o-C}_6\text{H}_4\text{O}_2$ at $\phi = 0.5$ are also very similar to those in the $\phi = 1.5$ oxidation, thus will not be discussed herein.

By comparing the JSR oxidation at 1 and 10 atm and at different equivalence ratios, the following conclusion can be drawn:

- (a) At 1 atm, A1CH_3 is mainly consumed by the H-atom abstraction reactions by H, OH and O. At $\phi = 1.5$, the H-atom abstraction reactions by H consume most of toluene. As equivalence ratio decreases, the roles of OH and O become significant; and at $\phi = 0.5$, the H-atom abstraction reactions by OH and O finally become dominant. At 10 atm and three equivalence ratios, the consumption of A1CH_3 is dominated by the H-atom abstraction reactions by OH and O.
- (b) The major consumption pathways of A1CH_2 are very different between 1 and 10 atm. At 1 atm and $\phi = 1.0$ and 1.5, most of A1CH_2 is consumed to form A1CH_3 and $\text{C}_6\text{H}_4\text{CH}_3$. While at 1 atm and $\phi = 0.5$ and at 10 atm, most of A1CH_2 is oxidized by HO_2 and O to form $\text{A1CH}_2\text{O}$. The reaction between A1CH_2 and HO_2 becomes more significant for A1CH_2 consumption as the equivalence ratio decreases at 10 atm and contributes over half of A1CH_2 consumption at the lean condition.
- (c) The chemistry of $\text{C}_6\text{H}_4\text{CH}_3$ plays a more important role at 1 atm than at 10 atm. This can be explained by that generally the temperatures at 1 atm are high enough for the formation of $\text{C}_6\text{H}_4\text{CH}_3$ from the isomerization reaction of A1CH_2 and H-atom abstraction reactions of A1CH_3 . The reaction sequence $\text{C}_6\text{H}_4\text{CH}_3 \rightarrow \text{o-C}_6\text{H}_4\text{O}_2 \rightarrow \text{C}_5\text{H}_4\text{O} \rightarrow \text{C}_4\text{H}_4$ ultimately leads to the production of vinylacetylene, and the reaction sequence $\text{C}_6\text{H}_4\text{CH}_3 \rightarrow \text{OC}_6\text{H}_4\text{CH}_3 \rightarrow \text{C}_5\text{H}_4\text{CH}_3 \rightarrow \text{fulvene} \rightarrow \text{A1}$ ultimately leads to the production of fulvene and benzene.

Furthermore, the Metcalfe model [29] and the Narayanaswamy model [7] were also used to simulate the oxidation of toluene at 10 atm and at $\phi = 0.5, 1.0$ and 1.5 in comparison with the present

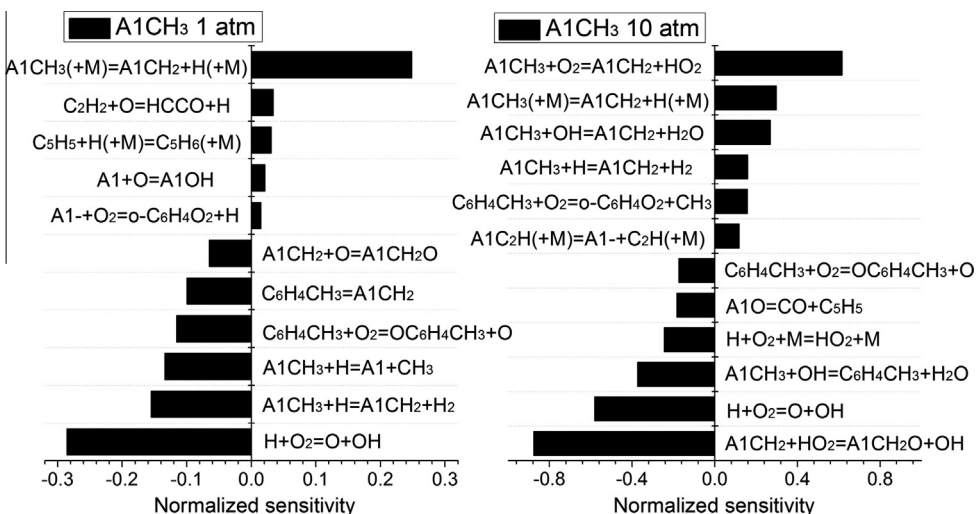


Fig. 19. Sensitivity analysis of toluene in the JSR oxidation of toluene at 1 atm, $\phi = 1.50$, 1350 K and 10 atm, $\phi = 1.50$, 1100 K.

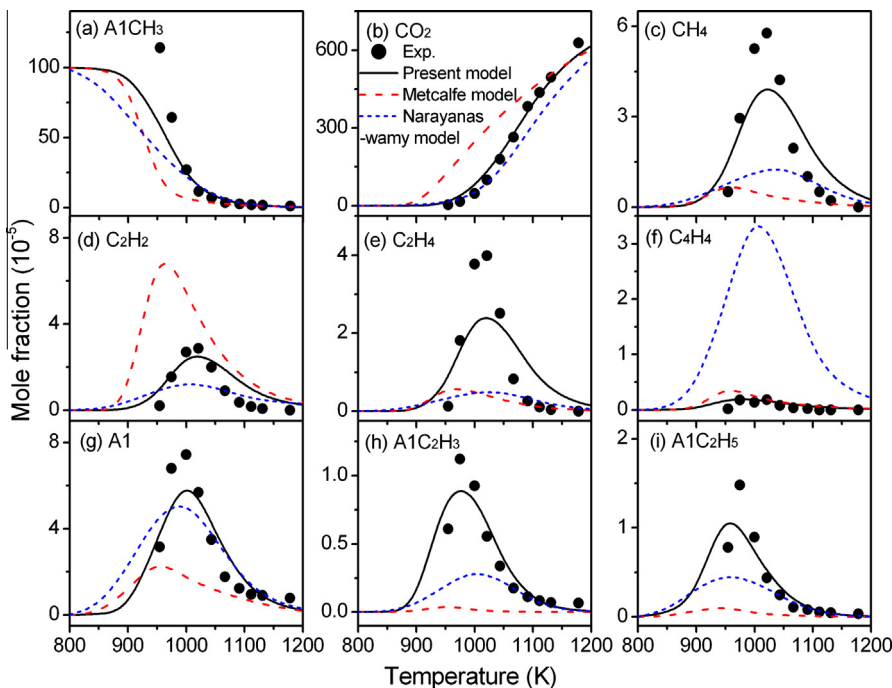


Fig. 20. Experimental (symbols) and simulated (lines) mole fractions of toluene ($A1CH_3$), carbon dioxide (CO_2), methane (CH_4), acetylene (C_2H_2), ethylene (C_2H_4), vinylacetylene (C_4H_4), benzene ($A1$), styrene ($A1C_2H_3$) and ethylbenzene ($A1C_2H_5$) in the JSR oxidation of toluene at 10 atm and $\phi = 0.50$ using the present model, Metcalfe model [29] and Narayanaswamy model [7].

model. Figure 20 illustrates the comparison of experimental and simulated mole fraction profiles of some selected species in the toluene oxidation at $\phi = 0.5$. Both the present model and Narayanaswamy model can capture the reactivity of toluene above 1000 K, while the Narayanaswamy model over-predicts the reactivity of toluene below 1000 K. The Metcalfe model over-predicts the reactivity of toluene at all temperatures by about 50 K. It also over-predicts the profiles of CO_2 and C_2H_2 , but under-predicts the profiles of CH_4 , C_2H_4 , $A1$, $A1C_2H_3$ and $A1C_2H_5$. The Narayanaswamy model highly over-predicts the profiles of C_4H_4 and under-predicts the profiles of CH_4 , C_2H_4 , $A1C_2H_3$ and $A1C_2H_5$. The comparisons at $\phi = 1.0$ and 1.5 are illustrated in Figs. S4 and S5 in Supplementary Materials, respectively. Both previous models over-predict the reactivity of toluene.

5. Conclusions

The flow reactor pyrolysis of toluene was studied at pressures from 5 to 760 Torr and temperatures from 1100 to 1730 K using SVUV-PIMS. The jet stirred reactor oxidation of toluene was investigated at the pressure of 10 atm, residence time of 0.6 s, equivalence ratios of 0.5, 1.0 and 1.5, and temperatures from 950 to 1200 K using GC. For the flow reactor pyrolysis, a number of pyrolysis products were detected, such as free radicals, isomers and PAHs. Their mole fraction profiles were evaluated as the function of heating temperature. For the JSR oxidation, the mole fractions of oxidation products were also evaluated as the function of heating temperature. A kinetic model was developed based on the recent theoretical progresses and was validated against the new flow reactor pyrolysis and JSR oxidation data, as well as the previous JSR oxidation data at 1 atm. By performing the ROP analysis and the sensitivity analysis, the key reaction networks were revealed for the investigated toluene pyrolysis and oxidation.

In the flow reactor pyrolysis, toluene is mainly consumed by H-atom abstraction and unimolecular decomposition reactions,

producing $A1CH_2$. The subsequent decomposition of $A1CH_2$ produces C_7H_6 , o - C_6H_4 , $A1$ and C_5H_6 . These products either decompose to smaller products or participate in the formation of PAHs. The important reactions for the formation and consumption of some large MAHs and typical PAHs were also discussed. It is concluded that $A1CH_2$, C_7H_5 , $A1$ - and C_5H_5 radicals, especially the two C_7 radicals, play important roles in the formation of PAHs.

In the JSR oxidation, toluene is mainly consumed by H-atom abstraction reactions by OH, H and O to produce $A1CH_2$. The dominant consumption pathways of toluene and $A1CH_2$ demonstrate some differences at 1 and 10 atm and at different equivalence ratios. Moreover, $C_6H_4CH_3$ radical plays a less important role at 10 atm than at 1 atm, and its oxidation sequence ultimately leads to C_4H_4 and $A1$.

Acknowledgments

The research at USTC leading to these results has received funding from National Natural Science Foundation of China (51106146), National Basic Research Program of China (973 Program) (2013CB834602), Anhui Provincial Natural Science Foundation (1408085J09), Fundamental Research Funds for the Central Universities (WK2320000020, WK2320000028) and Chinese Academy of Sciences. The research at CNRS leading to these results has received funding from the European Research Council under the European Community's Seventh Framework Programme (FP7/2007-2013)/ERC Grant Agreement No. 291049 – 2G-CSafe. We are also grateful to Mr. Zhandong Wang, Yizun Wang and Alexandre Marchal for technical assistance.

Appendix A. Supplementary material

Supplementary data associated with this article can be found, in the online version, at <http://dx.doi.org/10.1016/j.combustflame.2014.07.009>.

References

- [1] C.S. McEnally, L.D. Pfefferle, B. Atakan, K. Kohse-Höninghaus, *Prog. Energy Combust. Sci.* 32 (2006) 247–294.
- [2] J. Wang, B. Yang, Y.Y. Li, Z.Y. Tian, T.C. Zhang, F. Qi, K. Nakajima, *Int. J. Mass Spectrom.* 263 (2007) 30–37.
- [3] P. Dagaut, C. Togbé, *Energy Fuels* 22 (2008) 3499–3505.
- [4] T. Bielefeld, A. Frassoldati, A. Cuoci, T. Faravelli, E. Ranzi, U. Niemann, K. Seshadri, *Proc. Combust. Inst.* 32 (2009) 493–500.
- [5] Y.Y. Li, L.D. Zhang, T. Yuan, K.W. Zhang, J.Z. Yang, B. Yang, F. Qi, C.K. Law, *Combust. Flame* 157 (2010) 143–154.
- [6] Y.Y. Li, J.H. Cai, L.D. Zhang, T. Yuan, K.W. Zhang, F. Qi, *Proc. Combust. Inst.* 33 (2011) 593–600.
- [7] K. Narayanaswamy, G. Blanquart, H. Pitsch, *Combust. Flame* 157 (2010) 1879–1898.
- [8] A. Matsugi, A. Miyoshi, *Proc. Combust. Inst.* 34 (2013) 269–277.
- [9] R.D. Smith, *J. Phys. Chem.* 83 (1979) 1553–1563.
- [10] K.M. Pamidimukkala, R.D. Kern, M.R. Patel, H.C. Wei, J.H. Kiefer, *J. Phys. Chem.* 91 (1987) 2148–2154.
- [11] M.B. Colket, D.J. Seery, *Proc. Combust. Inst.* 25 (1994) 883–891.
- [12] R.A. Eng, A. Gebert, E. Goos, H. Hippler, C. Kachiani, *Phys. Chem. Chem. Phys.* 4 (2002) 3989–3996.
- [13] R. Sivaramakrishnan, R.S. Tranter, K. Brezinsky, *J. Phys. Chem. A* 110 (2006) 9388–9399.
- [14] R. Sivaramakrishnan, R.S. Tranter, K. Brezinsky, *J. Phys. Chem. A* 110 (2006) 9400–9404.
- [15] M.A. Oehlschlaeger, D.F. Davidson, R.K. Hanson, *Proc. Combust. Inst.* 31 (2007) 211–219.
- [16] T.C. Zhang, L.D. Zhang, X. Hong, K.W. Zhang, F. Qi, C.K. Law, T.H. Ye, P.H. Zhao, Y.L. Chen, *Combust. Flame* 156 (2009) 2071–2083.
- [17] F. Lannuzel, R. Bounaceur, R. Michels, G. Scacchi, P.-M. Marquaire, *J. Anal. Appl. Pyrol.* 87 (2010) 236–247.
- [18] L.D. Zhang, J.H. Cai, T.C. Zhang, F. Qi, *Combust. Flame* 157 (2010) 1686–1697.
- [19] B. Shukla, A. Susa, A. Miyoshi, M. Koshi, *J. Phys. Chem. A* 111 (2007) 8308–8324.
- [20] K. Brezinsky, T.A. Litzinger, I. Glassman, *Int. J. Chem. Kinet.* 16 (1984) 1053–1074.
- [21] K. Brezinsky, A.B. Lovell, I. Glassman, *Combust. Sci. Technol.* 70 (1990) 33–46.
- [22] J.L. Endee, K. Brezinsky, I. Glassman, *J. Phys. Chem.* 96 (1992) 2151–2161.
- [23] S.D. Klotz, K. Brezinsky, I. Glassman, *Proc. Combust. Inst.* 27 (1998) 337–344.
- [24] P. Dagaut, G. Pengloan, A. Ristori, *Phys. Chem. Chem. Phys.* 4 (2002) 1846–1854.
- [25] L.D. Costa, R. Fournet, F. Billaud, F. Battin-Leclerc, *Int. J. Chem. Kinet.* 35 (2003) 503–524.
- [26] R. Sivaramakrishnan, R.S. Tranter, K. Brezinsky, *Combust. Flame* 139 (2004) 340–350.
- [27] R. Bounaceur, I. Da Costa, R. Fournet, F. Billaud, F. Battin-Leclerc, *Int. J. Chem. Kinet.* 37 (2005) 25–49.
- [28] R. Sivaramakrishnan, R.S. Tranter, K. Brezinsky, *Proc. Combust. Inst.* 30 (2005) 1165–1173.
- [29] W.K. Metcalfe, S. Dooley, F.L. Dryer, *Energy Fuels* 25 (2011) 4915–4936.
- [30] A. Hamins, K. Seshadri, *Combust. Flame* 68 (1987) 295–307.
- [31] V. Detilleux, J. Vandooren, *J. Phys. Chem. A* 113 (2009) 10913–10922.
- [32] Y.Y. Li, L.D. Zhang, Z.Y. Tian, T. Yuan, J. Wang, B. Yang, F. Qi, *Energy Fuels* 23 (2009) 1473–1485.
- [33] V. Detilleux, J. Vandooren, *Proc. Combust. Inst.* 33 (2011) 217–224.
- [34] A. Burcat, C. Snyder, T. Brabbs, Ignition Delay Times of Benzene and Toluene with Oxygen in Argon Mixtures, NASA Technical Memorandum 87312, 1986.
- [35] G. Pengloan, P. Dagaut, N. Djebaili-Chaumeix, C.E. Paillard, M. Cathonnet, in: Proceedings of the Colloque Combustion Propre, Orleans, France, 2001.
- [36] D.F. Davidson, B.M. Gauthier, R.K. Hanson, *Proc. Combust. Inst.* 30 (2005) 1175–1182.
- [37] V. Vasudevan, D.F. Davidson, R.K. Hanson, *Proc. Combust. Inst.* 30 (2005) 1155–1163.
- [38] G. Mittal, C.-J. Sung, *Combust. Flame* 150 (2007) 355–368.
- [39] H.-P.S. Shen, J. Vanderover, M.A. Oehlschlaefer, *Proc. Combust. Inst.* 32 (2009) 165–172.
- [40] S.S. Vasu, D.F. Davidson, R.K. Hanson, *J. Propul. Power* 26 (2010) 776–783.
- [41] S.G. Davis, C.K. Law, *Combust. Sci. Technol.* 140 (1998) 427–449.
- [42] T. Hirasawa, C.-J. Sung, A. Joshi, Z. Yang, H. Wang, C.K. Law, *Proc. Combust. Inst.* 29 (2002) 1427–1434.
- [43] K. Kumar, J.E. Freeh, C.J. Sung, Y. Huang, *J. Propul. Power* 23 (2007) 428–436.
- [44] X. Hui, A.K. Das, K. Kumar, C.-J. Sung, S. Dooley, F.L. Dryer, *Fuel* 97 (2012) 695–702.
- [45] C.S. Ji, E. Dames, H. Wang, F.N. Egolfopoulos, *Combust. Flame* 159 (2012) 1070–1081.
- [46] L. Sileghem, V.A. Alekseev, J. Vancoillie, K.M. Van Geem, E.J.K. Nilsson, S. Verhelst, A.A. Konnov, *Fuel* 112 (2013) 355–365.
- [47] R.J. Johnston, J.T. Farrell, *Proc. Combust. Inst.* 30 (2005) 217–224.
- [48] E. Ranzi, A. Frassoldati, R. Grana, A. Cuoci, T. Faravelli, A.P. Kelley, C.K. Law, *Prog. Energy Combust. Sci.* 38 (2012) 468–501.
- [49] T. Seto, M. Nakajima, A. Miyoshi, *J. Phys. Chem. A* 110 (2006) 5081–5090.
- [50] S.J. Klippenstein, L.B. Harding, Y. Georgievskii, *Proc. Combust. Inst.* 31 (2007) 221–229.
- [51] G. da Silva, J.W. Bozzelli, *J. Phys. Chem. A* 113 (2009) 12045–12048.
- [52] G. da Silva, J.W. Bozzelli, *Proc. Combust. Inst.* 32 (2009) 287–294.
- [53] G. da Silva, J.A. Cole, J.W. Bozzelli, *J. Phys. Chem. A* 113 (2009) 6111–6120.
- [54] G. da Silva, J.A. Cole, J.W. Bozzelli, *J. Phys. Chem. A* 114 (2010) 2275–2283.
- [55] G. da Silva, A.J. Trevitt, *Phys. Chem. Chem. Phys.* 13 (2011) 8940–8952.
- [56] G. da Silva, A.J. Trevitt, M. Steinbauer, P. Hemberger, *Chem. Phys. Lett.* 517 (2011) 144–148.
- [57] M. Derudi, D. Polino, C. Cavallotti, *Phys. Chem. Chem. Phys.* 13 (2011) 21308–21318.
- [58] B. Lefort, W. Tsang, *Combust. Flame* 158 (2011) 657–665.
- [59] D. Polino, C. Cavallotti, *J. Phys. Chem. A* 115 (2011) 10281–10289.
- [60] D. Polino, A. Famulari, C. Cavallotti, *J. Phys. Chem. A* 115 (2011) 7928–7936.
- [61] C. Cavallotti, D. Polino, A. Frassoldati, E. Ranzi, *J. Phys. Chem. A* 116 (2012) 3313–3324.
- [62] Y.Y. Li, F. Qi, *Acc. Chem. Res.* 43 (2009) 68–78.
- [63] J.H. Cai, L.D. Zhang, F. Zhang, Z.D. Wang, Z.J. Cheng, W.H. Yuan, F. Qi, *Energy Fuels* 26 (2012) 5550–5568.
- [64] F. Qi, *Proc. Combust. Inst.* 34 (2013) 33–63.
- [65] Y.J. Zhang, J.H. Cai, L. Zhao, J.Z. Yang, H.F. Jin, Z.J. Cheng, Y.Y. Li, L.D. Zhang, F. Qi, *Combust. Flame* 159 (2012) 905–917.
- [66] C.R. Narayanan, S. Srinivasan, A.K. Datye, R. Gorte, A. Biaglow, *J. Catal.* 138 (1992) 659–674.
- [67] D.S. Maciver, H.H. Tobin, R.T. Barth, *J. Catal.* 2 (1963) 485–497.
- [68] M. Cathonnet, J.C. Boettner, H. James, *Proc. Combust. Inst.* 18 (1981) 903–913.
- [69] P. Glarborg, P.G. Kristensen, S.H. Jensen, K. Dam-Johansen, *Combust. Flame* 98 (1994) 241–258.
- [70] P.G. Kristensen, P. Glarborg, K. Dam-Johansen, *Combust. Flame* 107 (1996) 211–222.
- [71] Photonionization Cross Section Database (Version 1.0), National Synchrotron Radiation Laboratory, Hefei, China, 2011, <<http://flame.nsrl.ustc.edu.cn/en/database.htm>>.
- [72] P. Dagaut, M. Reuillon, M. Cathonnet, *Combust. Flame* 101 (1995) 132–140.
- [73] R. Sivaramakrishnan, J.V. Michael, *Proc. Combust. Inst.* 33 (2011) 225–232.
- [74] H. Wang, M. Frenklach, *Combust. Flame* 110 (1997) 173–221.
- [75] M.A. Oehlschlaefer, D.F. Davidson, R.K. Hanson, *J. Phys. Chem. A* 110 (2006) 9867–9873.
- [76] G. Blanquart, P. Pepiot-Desjardins, H. Pitsch, *Combust. Flame* 156 (2009) 588–607.
- [77] C.A. Taatjes, D.L. Osborn, T.M. Selby, G. Meloni, A.J. Trevitt, E. Epifanovsky, A.I. Krylov, B. Sirjean, E. Dames, H. Wang, *J. Phys. Chem. A* 114 (2010) 3355–3370.
- [78] M.A. Oehlschlaefer, D.F. Davidson, R.K. Hanson, *Combust. Flame* 147 (2006) 195–208.
- [79] D.L. Baulch, C.T. Bowman, C.J. Cobos, R.A. Cox, T. Just, J.A. Kerr, M.J. Pilling, D. Stocker, J. Troe, W. Tsang, R.W. Walker, J. Warnatz, *J. Phys. Chem. Ref. Data* 34 (2005) 1575–1397.
- [80] M. Altarawneh, B.Z. Dlugogorski, E.M. Kennedy, J.C. Mackie, *Combust. Flame* 157 (2010) 1325–1330.
- [81] C. Cavallotti, M. Derudi, R. Rota, Decomposition of the Benzyl Radical through C7H6 Species, in: Proceedings of the Italian Section of the Combustion Institute, 2007, pp. I-2, 1-I-2, 6.
- [82] C. Cavallotti, M. Derudi, R. Rota, *Proc. Combust. Inst.* 32 (2009) 115–121.
- [83] R. Sivaramakrishnan, M.C. Su, J.V. Michael, *Proc. Combust. Inst.* 33 (2011) 243–250.
- [84] Y. Murakami, T. Oguchi, K. Hashimoto, Y. Nosaka, *J. Phys. Chem. A* 111 (2007) 13200–13208.
- [85] G. da Silva, J.W. Bozzelli, *J. Phys. Chem. A* 113 (2009) 6979–6986.
- [86] L.K. Madden, L.V. Moskaleva, S. Kristyan, M.C. Lin, *J. Phys. Chem. A* 101 (1997) 6790–6797.
- [87] E. Dames, H. Wang, *Proc. Combust. Inst.* 34 (2013) 307–314.
- [88] G. da Silva, C.-C. Chen, J.W. Bozzelli, *J. Phys. Chem. A* 111 (2007) 8663–8676.
- [89] X.Q. You, D.Y. Zubarev, W.A. Lester, M. Frenklach, *J. Phys. Chem. A* 115 (2011) 14184–14190.
- [90] S.G. Davis, H. Wang, K. Brezinsky, C.K. Law, *Proc. Combust. Inst.* 26 (1996) 1025–1033.
- [91] B. Shukla, M. Koshi, *Combust. Flame* 158 (2011) 369–375.
- [92] L. Vereecken, H.F. Bettinger, J. Peeters, *Phys. Chem. Chem. Phys.* 4 (2002) 2019–2027.
- [93] L. Vereecken, J. Peeters, *Phys. Chem. Chem. Phys.* 5 (2003) 2807–2817.
- [94] V.V. Kislov, A.M. Mebel, *J. Phys. Chem. A* 112 (2008) 700–716.
- [95] A. Matsugi, A. Miyoshi, *Int. J. Chem. Kinet.* 44 (2012) 206–218.
- [96] H. Richter, S. Granata, W.H. Green, J.B. Howard, *Proc. Combust. Inst.* 30 (2005) 1397–1405.
- [97] D. Wang, A. Violi, D.H. Kim, J.A. Mullholland, *J. Phys. Chem. A* 110 (2006) 4719–4725.
- [98] A.M. Mebel, V.V. Kislov, *J. Phys. Chem. A* 113 (2009) 9825–9833.
- [99] A. Comandini, T. Malewicki, K. Brezinsky, *J. Phys. Chem. A* 116 (2012) 2409–2434.
- [100] R.S. Tranter, S.J. Klippenstein, L.B. Harding, B.R. Giri, X. Yang, J.H. Kiefer, *J. Phys. Chem. A* 114 (2010) 8240–8261.
- [101] B. Shukla, K. Tsuchiya, M. Koshi, *J. Phys. Chem. A* 115 (2011) 5284–5293.
- [102] A. Matsugi, A. Miyoshi, *Phys. Chem. Chem. Phys.* 14 (2012) 9722.
- [103] H. Wang, X. You, A.V. Joshi, S.G. Davis, A. Laskin, F. Egolfopoulos, C.K. Law, High-Temperature Combustion Reaction Model of H2/CO/C1–C4 Compounds, 2007, <http://ignis.usc.edu/USC_Mech_II.htm>.
- [104] J.H. Cai, W.H. Yuan, L.L. Ye, Z.J. Cheng, Y.Z. Wang, L.D. Zhang, F. Zhang, Y.Y. Li, F. Qi, *Combust. Flame* 160 (2013) 1939–1957.
- [105] G. Blanquart, H. Pitsch, *J. Phys. Chem. A* 111 (2007) 6510–6520.
- [106] CHEMKIN-PRO 15092, Reaction Design: San Diego, 2009.
- [107] Y.R. Luo, Comprehensive Handbook of Chemical Bond Energies, CRC Press, Boca Raton, FL, 2007.
- [108] S. Sharma, W.H. Green, *J. Phys. Chem. A* 113 (2009) 8871–8882.
- [109] C. Cavallotti, D. Polino, Proc. Combust. Inst. 34 (2013) 557–564.
- [110] H. Richter, J.B. Howard, *Phys. Chem. Chem. Phys.* 4 (2002) 2038–2055.